

HATS-39b, HATS-40b, HATS-41b, AND HATS-42b: THREE INFLATED HOT JUPITERS AND A SUPER-JUPITER TRANSITING F STARS

J. BENTO,¹ J. D. HARTMAN,² G. Á. BAKOS,² W. BHATTI,² Z. CSUBRY,² K. PENEV,^{2,3} D. BAYLISS,⁴ M. DE VAL-BORRO,⁵ G. ZHOU,⁶ R. BRAHM,^{7,8} N. ESPINOZA,⁹ M. RABUS,^{8,9} A. JORDÁN,^{8,7,9} V. SUC,⁸ S. CICERI,⁹ P. SARKIS,⁹ T. HENNING,⁹ L. MANCINI,^{10,9,11} C. G. TINNEY,^{12,13} D. J. WRIGHT,^{12,13} S. DURKAN,¹⁴ T. G. TAN,¹⁵ J. LÁZÁR,¹⁶ I. PAPP,¹⁶ AND P. SÁRI¹⁶

¹Research School of Astronomy and Astrophysics, Mount Stromlo Observatory, Australian National University, Cotter Road, Weston, ACT 2611, Australia. E-mail: joao.bento@anu.edu.au

²Department of Astrophysical Sciences, 4 Ivy Ln., Princeton, NJ 08544

³Physics Department, University of Texas at Dallas, 800 W Campbell Rd. MS WT15, Richardson, TX 75080, USA

⁴Department of Physics, University of Warwick, Coventry CV4 7AL, UK

⁵Astrochemistry Laboratory, Goddard Space Flight Center, NASA, 8800 Greenbelt Rd, Greenbelt, MD 20771, USA

⁶Harvard-Smithsonian Center for Astrophysics, Cambridge, MA 02138, USA

⁷Millennium Institute for Astrophysics, Santiago, Chile

⁸Instituto de Astrofísica, Facultad de Física, Pontificia Universidad Católica de Chile, Vicuña Mackenna 4860, 7820436 Macul, Santiago, Chile

⁹Max Planck Institute for Astronomy, Königstuhl 17, 69117 Heidelberg, Germany

¹⁰Department of Physics, University of Rome Tor Vergata, Via della Ricerca Scientifica 1, 00133 Roma, Italy

¹¹INAF – Astrophysical Observatory of Turin, Via Osservatorio 20, 10025 – Pino Torinese, Italy

¹²Exoplanetary Science at UNSW, School of Physics UNSW Sydney, NSW 2052, Australia

¹³Australian Centre for Astrobiology, School of Physics, UNSW Sydney, NSW 2052, Australia

¹⁴Astrophysics Research Centre, Queens University, Belfast, Belfast, Northern Ireland, UK

¹⁵Perth Exoplanet Survey Telescope, Perth, Australia

¹⁶Hungarian Astronomical Association, 1451 Budapest, Hungary

ABSTRACT

We report the discovery of four transiting hot Jupiters from the HATSouth survey: HATS-39b, HATS-40b, HATS-41b and HATS-42b. These discoveries add to the growing number of transiting planets orbiting moderately bright ($12.5 \lesssim V \lesssim 13.7$) F dwarf stars on short (2-5 day) periods. The planets have similar radii, ranging from $1.33^{+0.29}_{-0.20} R_J$ for HATS-41b to $1.58^{+0.16}_{-0.12} R_J$ for HATS-40b. Their masses and bulk densities, however, span more than an order of magnitude. HATS-39b has a mass of $0.63 \pm 0.13 M_J$, and an inflated radius of $1.57 \pm 0.12 R_J$, making it a good target for future transmission spectroscopic studies. HATS-41b is a very massive $9.7 \pm 1.6 M_J$ planet and one of only a few hot Jupiters found to date with a mass over $5 M_J$. This planet orbits the highest metallicity star ($[Fe/H] = 0.470 \pm 0.010$) known to host a transiting planet and is also likely on an eccentric orbit. The high mass, coupled with a relatively young age ($1.34^{+0.31}_{-0.51}$ Gyr) for the host star, are factors that may explain why this planet's orbit has not yet circularised.

Keywords: planetary systems — stars: individual (HATS-39, GSC 6550-00341, HATS-40, GSC 6533-01514 HATS-41, GSC 6530-01596 HATS-42, GSC 7107-03973) techniques: spectroscopic, photometric

1. INTRODUCTION

Planets that transit their host star are key for understanding the details of planet formation, structure and evolution. These systems not only provide a unique opportunity for further studies of atmospheric and surface conditions (e.g. Bento et al. 2014; Jordán et al. 2013; Sing et al. 2011; Zhou et al. 2014; Désert et al. 2011; Louden & Wheatley 2015), but are also the exoplanets for which two complementary measurement techniques (i.e. transit photometry and host-star radial velocity) can be combined to deliver both planet mass and planet radius, so yielding a measurement of bulk planet density. The vast majority of well-characterised exoplanets to date have been discovered using wide-field photometric surveys, either from the ground (e.g. HATNet, Bakos et al. (2004) and SuperWASP, Pollacco et al. (2006)) or space (e.g. Kepler and K2, Borucki et al. 2010).

In particular, hot Jupiters (broadly defined as Jupiter-mass planets orbiting close to their host stars with orbital periods less than ~ 10 days) are still challenging models of planetary formation and evolution, despite over twenty years of study. The general consensus is that these planets are formed at large separations and migrate inwards to their current positions. There is, however, no consensus yet as to how these planets migrate, with a variety of mechanisms having been proposed (e.g. Chambers 2009; Ford & Rasio 2008; Wu & Murray 2003; Petrovich 2015, and references therein). The increasing number of discoveries is now allowing studies that can statistically test the significance of these mechanisms – for example investigating the dependence of eccentricity on mass and orbital separation (Mazeh et al. 1997; Southworth et al. 2009; Pont et al. 2011), to determine which migration mechanism (if any) is dominant. If planet-planet scattering dominates over disk migration, then it would be reasonable to expect eccentric planets at large separations in young systems. This drives the need to discover larger samples of planets spanning a larger range of ages and orbital separations.

In this paper we report the discovery and characterisation of four new transiting hot Jupiters from the HATSouth survey: HATS-39b, HATS-40b, HATS-41b and HATS-42b. In Section 2 we describe the photometric and spectroscopic observations undertaken for all four targets. Section 3 contains a description of the global data analysis and presents the modelled stellar and planetary parameters. We also describe the methods employed to reject false positive scenarios. Our findings are finally discussed in Section 4.

2. OBSERVATIONS

A range of astrophysical events can mimic the photometric transit events for an exoplanet in a wide-field survey. These include grazing eclipses in binary systems, transiting late-M dwarfs, eclipses by dwarf star companions of evolved primary stars and eclipsing binary star systems whose light is blended with a third unresolved star. Substantial follow-up campaigns are required to obtain the additional photometric and spectroscopic observations required to reject these contaminants and confirm the planetary nature of the candidates found by the survey.

2.1. Photometric detection

The HATSouth project is an ongoing effort by a number of collaborating institutions¹ aimed at discovering transiting planets orbiting moderately bright stars visible from the southern hemisphere (Bakos et al. 2013). It is composed of three identical facilities at Las Campanas Observatory in Chile, the High Energy Spectroscopic Survey (HESS) site in Namibia, and Siding Spring Observatory, Australia. The longitudinal coverage of these sites means that together they can continuously monitor 128 sq degree fields in the southern sky. This is highlighted by the discovery of HATS-17b (Brahm et al. 2016), the longest period transiting exoplanet found to date by a wide-field ground-based survey. A full list of discovered planets along with corresponding discovery light curves can be found at <https://hatsouth.org/>.

Table 1 shows a summary of the HATSouth photometric observations for the four new exoplanetary systems described in the present work (along with observing details for subsequent follow-up observations with the Las Cumbres Observatory Global Telescope (LCOGT) and the 0.3 m PEST telescope in Western Australia – see Section 2.3). For HATSouth data, we list the HATSouth unit, CCD and field name from which the observations were taken. The detection of all targets relied on data from all HATSouth telescopes. The HATSouth data for these targets spans a period of just under two years, from August 2011 to April 2013, resulting in a total of 16,488 data points for HATS-39, 27,476 for HATS-40, 11,938 for HATS-41, and 21,210 for HATS-42.

¹ The HATSouth network is operated by a collaboration consisting of Princeton University (PU), the Max Planck Institute für Astronomie (MPIA), the Australian National University (ANU), and the Pontificia Universidad Católica de Chile (PUC). The station at Las Campanas Observatory (LCO) of the Carnegie Institute is operated by PU in conjunction with PUC, the station at the High Energy Spectroscopic Survey (H.E.S.S.) site is operated in conjunction with MPIA, and the station at Siding Spring Observatory (SSO) is operated jointly with ANU.

All HATSouth observations are obtained through a Sloan r filter with a typical cadence of 4 minutes. The data were reduced with a custom pipeline described by Penev et al. (2013), and light curves were de-trended using an External Parameter Decorrelation method (Bakos et al. 2010), followed by the application of a Trend Filtering Algorithm (TFA, Kovács et al. 2005). The Box-fitting Least-Squares algorithm (BLS; see Kovács et al. 2002) was then used to search for periodic transit-like signals. The resulting discovery light curves are shown in Figure 1, phase-folded to the highest likelihood periods. This figure contains both the full phase light curves for all four systems, as well as an expanded section around the transit, binned data points and the best fit model. Clear transit signals are readily visible. We highlight the case of HATS-40 where the apparent transit depth is ~ 4.7 mmag, which is comparable to the smallest transit depths of previous HATSouth discovered planets (HATS-9b, HATS-12b and HATS-17b Brahm et al. 2015; Rabus et al. 2016; Brahm et al. 2016, respectively). HATSouth is able to consistently detect transit signals of a few mmag depth for its target magnitude range down to $V = 15$.

After having removed the best fit Box Least Squares model corresponding to the hot-Jupiter transit signal from the light curves, we searched for additional periodic signals in an attempt to identify other transiting planets or potential stellar photometric activity. None of the light curves revealed any other significant signals, where

“significant” is defined by the formal false alarm probability (assuming Gaussian white noise, of less than 0.1%) on a second BLS pass of the residuals. Additionally, a Generalised Lomb Scargle (GLS, Zechmeister & Kürster 2009) search for sinusoidal patterns related to stellar activity (either in the form of spots or pulsations) detected no significant periodic signals. We conclude there is no evidence for additional transiting planets in the systems, or clear evidence of photometric activity in the host stars. We note, additionally, that three of our targets were present in overlapping regions for multiple cameras on the same site, and therefore were observed by multiple cameras simultaneously. This further adds to a robust photometric signal where some systematic errors are averaged out by data combination from multiple sources. Depending on the characteristics and sampling of the light curves under analysis, the process of applying the TFA algorithm occasionally removes astrophysical signals that may have an impact on the conclusions regarding each system. We therefore looked for periodic signals in the pre-TFA light curves. A sinusoidal signal with a period of 29.04 days is detected with a false alarm probability of 10^{-12} in the light curve for HATS-39. The false alarm probability is based on bootstrap simulations. This signal is most likely an instrumental artifact associated with systematic variations in the sky background corresponding the lunar orbital period. No other significant periodic signals are found in the light curves of the remaining targets.

Table 1. Summary of photometric observations

Instrument/Field ^a	Date(s)	# Images	Cadence ^b (sec)	Filter	Precision ^c (mmag)
HATS-39					
HS-2.3/G602	2011 Aug–2012 Feb	4942	295	r	9.0
HS-4.3/G602	2011 Aug–2012 Feb	1835	304	r	8.9
HS-6.3/G602	2011 Oct–2012 Feb	1362	302	r	10.4
HS-2.4/G602	2011 Aug–2012 Feb	4098	295	r	11.2
HS-4.4/G602	2011 Aug–2012 Feb	3044	296	r	9.2
HS-6.4/G602	2011 Oct–2012 Feb	1207	303	r	10.3
LCOGT 1 m+CTIO/sinistro	2015 Oct 23	67	159	i	1.6
LCOGT 1 m+SSO/SBIG	2015 Nov 11	53	132	i	2.1
LCOGT 1 m+SAAO/SBIG	2015 Dec 31	80	134	i	2.4
LCOGT 1 m+CTIO/sinistro	2016 Jan 09	122	159	i	1.1
Swope 1 m/e2v	2016 Jan 09	449	59	i	2.5
HATS-40					
HS-2.3/G600	2012 Sep–2013 Apr	7339	281	r	11.3

Table 1 continued

Table 1 (*continued*)

Instrument/Field ^a	Date(s)	# Images	Cadence ^b (sec)	Filter	Precision ^c (mmag)
HS-4.3/G600	2012 Sep–2013 Apr	2908	291	<i>r</i>	11.1
HS-6.3/G600	2012 Sep–2013 Jan	2954	289	<i>r</i>	10.8
HS-4.4/G600	2012 Sep–2013 Feb	2313	291	<i>r</i>	12.7
HS-6.4/G600	2012 Sep	3	...	<i>r</i>	17.9
HS-1.2/G601	2011 Aug–2012 Jan	4806	296	<i>r</i>	8.3
HS-3.2/G601	2011 Aug–2012 Jan	4072	296	<i>r</i>	8.5
HS-5.2/G601	2011 Aug–2012 Jan	3081	290	<i>r</i>	9.0
PEST 0.3 m	2014 Nov 07	88	133	R_C	4.2
LCOGT 1 m+SSO/SBIG	2015 Mar 08	69	196	<i>i</i>	3.5
LCOGT 1 m+SSO/SBIG	2015 Apr 13	54	195	<i>i</i>	3.2
LCOGT 1 m+CTIO/sinistro	2015 Sep 06	11	222	<i>i</i>	2.7
LCOGT 1 m+SAAO/SBIG	2015 Sep 13	28	194	<i>i</i>	2.7
LCOGT 1 m+SAAO/SBIG	2015 Oct 06	61	192	<i>i</i>	2.3
LCOGT 1 m+SAAO/SBIG	2015 Nov 04	27	192	<i>i</i>	2.0
LCOGT 1 m+SSO/SBIG	2015 Dec 07	79	192	<i>i</i>	3.1
LCOGT 1 m+CTIO/sinistro	2015 Dec 13	95	219	<i>i</i>	1.3
LCOGT 1 m+CTIO/SBIG	2015 Dec 23	107	192	<i>i</i>	2.8
LCOGT 1 m+SSO/SBIG	2015 Dec 30	8	193	<i>i</i>	1.9
LCOGT 1 m+SAAO/SBIG	2016 Jan 02	62	195	<i>i</i>	2.7
LCOGT 1 m+SAAO/SBIG	2016 Jan 05	55	192	<i>i</i>	4.2
HATS-41					
HS-1.2/G601	2011 Aug–2012 Jan	4790	296	<i>r</i>	6.5
HS-3.2/G601	2011 Aug–2012 Jan	4059	296	<i>r</i>	7.1
HS-5.2/G601	2011 Aug–2012 Jan	3089	290	<i>r</i>	6.3
LCOGT 1 m+CTIO/sinistro	2014 Nov 30	55	229	<i>i</i>	1.1
Swope 1 m/e2v	2014 Nov 30	171	99	<i>i</i>	1.8
LCOGT 1 m+CTIO/sinistro	2015 Sep 07	35	162	<i>i</i>	1.7
LCOGT 1 m+SAAO/SBIG	2015 Oct 15	65	137	<i>i</i>	1.9
HATS-42					
HS-1.4/G601	2011 Aug–2012 Jan	4840	296	<i>r</i>	10.2
HS-3.4/G601	2011 Aug–2012 Jan	4033	296	<i>r</i>	10.8
HS-5.4/G601	2011 Aug–2012 Jan	3075	290	<i>r</i>	10.2
HS-2.1/G602	2011 Aug–2012 Feb	5247	295	<i>r</i>	8.8
HS-4.1/G602	2011 Aug–2012 Feb	2621	297	<i>r</i>	9.9
HS-6.1/G602	2011 Oct–2012 Feb	1394	303	<i>r</i>	9.5
Swope 1 m/e2v	2016 Jan 08	181	99	<i>i</i>	2.3

^a For HATSouth data we list the HATSouth unit, CCD and field name from which the observations are taken. HS-1 and -2 are located at Las Campanas Observatory in Chile, HS-3 and -4 are located at the HESS site in Namibia, and HS-5 and -6 are located at Siding Spring Observatory in Australia. Each unit has 4 CCDs. Each field corresponds to one of 838 fixed pointings used to cover the full 4π celestial sphere. All data from a given HATSouth field and CCD number are reduced together, while detrending through External Parameter Decorrelation (EPD) is done independently for each unique unit+CCD+field combination.

^b The median time between consecutive images rounded to the nearest second. Due to factors such as weather, the day–night cycle, guiding and focus corrections the cadence is only approximately uniform over short timescales.

^c The RMS of the residuals from the best-fit model.

2.2. Spectroscopic Observations

In this section we describe our spectroscopic follow-up observations, from initial candidate vetting, through to orbital characterisation.

2.2.1. Reconnaissance spectroscopic observations

The initial follow-up phase for HATSouth planet candidates utilised spectra acquired with the WiFeS instrument on the 2.3m ANU telescope at Siding Spring Ob-

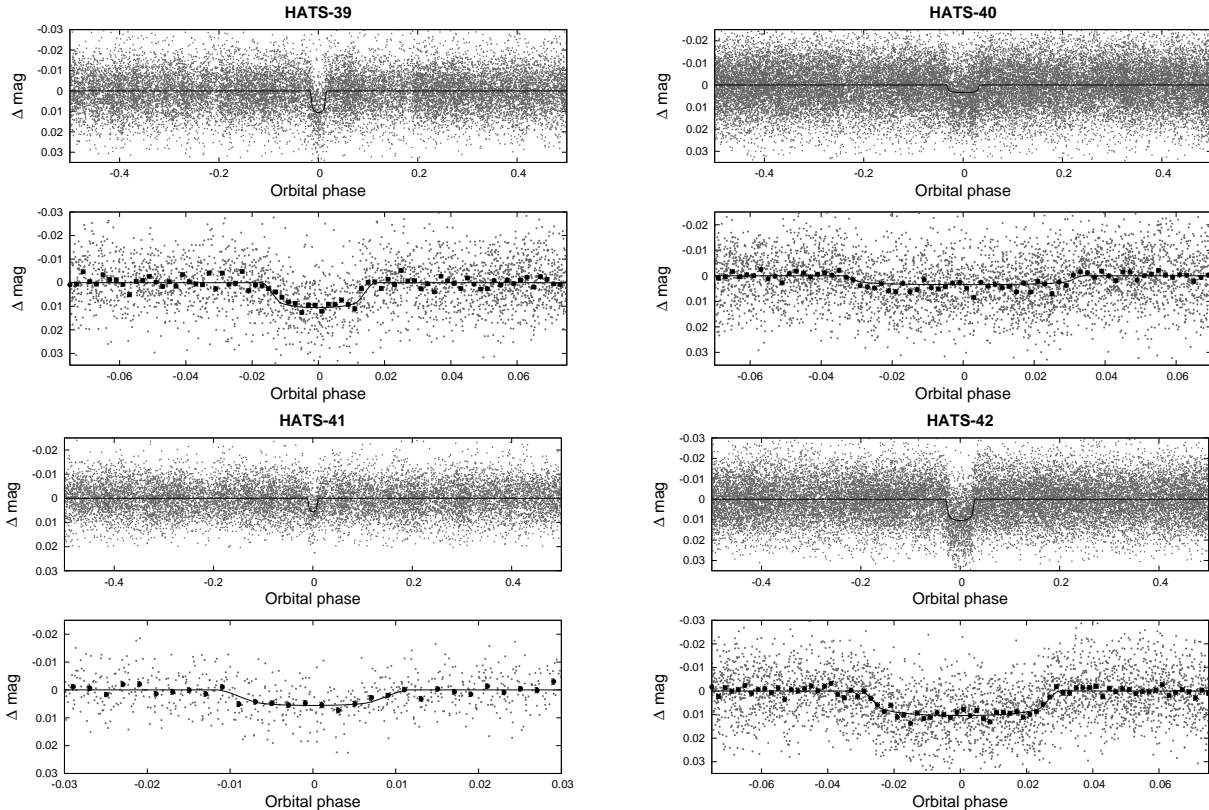


Figure 1. Phase-folded unbinned HATSouth light curves for HATS-39 (upper left), HATS-40 (upper right), HATS-41 (lower left) and HATS-42 (lower right). In each case we show two panels. The top panel shows the full light curve, while the bottom panel shows the light curve zoomed-in on the transit. The solid lines show the model fits to the light curves. The dark filled circles in the bottom panels show the light curves binned in phase with a bin size of 0.002.

servatory (SSO; Dopita et al. 2007). For our targets this combination delivers low-resolution spectra, over a wide wavelength range at high speed – upwards of 60 targets per night can be easily observed. The purpose of these reconnaissance observations is to quickly eliminate those systems whose detectable transits are clearly not from planets. Observations at $R \equiv \Delta\lambda/\lambda \approx 3000$ using the blue arm of the spectrograph are used to determine the stellar type of the host star. We estimate three key stellar properties, the effective temperature T_{eff} , $\log g_*$ and $[\text{Fe}/\text{H}]$ by performing a χ^2 minimisation grid search between each the observed, normalised spectrum and synthetic templates from the MARCS model atmospheres (Gustafsson et al. 2008). 2MASS J–K colors are used to restrict the T_{eff} parameter space and extinction correction is applied using the method of Cardelli et al. (1989). A detailed description of the observing and data reduction procedure is described in Bayliss et al. (2013). These data identify giant host stars, for which the observed dip in the light curve could only have been caused by a stellar companion, and to identify stars not suitable for precise radial velocity follow-up due to high T_{eff} or large $v \sin i$.

Targets not eliminated by these data are observed at predicted quadrature phases using a WiFES higher resolving power grating ($R \sim 7,000$) to obtain radial velocity measurements with $\sim 2\text{km s}^{-1}$ precision (the true precision varies depending on stellar type and signal-to-noise of each individual target). Radial velocities are measured by cross-correlation against velocity standards observed every night, calibrated using bracketed NeAr exposures and a selection of telluric lines. This allows the detection of radial velocity variations with amplitudes above $\sim 5\text{km s}^{-1}$, which indicate that the transiting companion is a star. The results of these initial vetting observations for our four targets are:

- HATS-39 has an effective temperature of $6460 \pm 300\text{K}$, $\log g_*$ of 3.9 ± 0.3 and metallicity of $[\text{Fe}/\text{H}] = -0.5 \pm 0.5$, leading to the conclusion that this is a F-dwarf host star. Two radial velocity measurements at each quadrature showed no significant variation.
- HATS-40 has an effective temperature of $6720 \pm 300\text{K}$, $\log g_*$ of 4.0 ± 0.3 and metallicity of $[\text{Fe}/\text{H}] = 0.0 \pm 0.5$. We conclude that the host star is an F

Table 2. Summary of spectroscopic observations

Instrument	UT Date(s)	# Spec.	Res. $\Delta\lambda/\lambda/1000$	S/N Range ^a	γ_{RV} ^b (km s^{-1})	Precision ^c (m s^{-1})
HATS-39						
ANU 2.3 m/WiFeS	2014 Feb 23	1	3	65
ANU 2.3 m/WiFeS	2014 Jun–Dec	3	7	7–82	1.2	4000
ESO 3.6 m/HARPS	2015 Feb–2016 Apr	17	115	15–31	2.916	39
AAT 3.9 m/CYCLOPS2+UCLES	2015 March 1	3	70	15–17	3.092	89
HATS-40						
ANU 2.3 m/WiFeS	2014 Oct 7	1	3	42
ANU 2.3 m/WiFeS	2014 Oct 8–11	2	7	14–24	9.8	4000
Euler 1.2 m/Coralie	2014 Oct–2015 Oct	6	60	10–14	9.30	460
ESO 3.6 m/HARPS	2015 Feb–Nov	10	115	6–17	9.194	49
HATS-41						
ANU 2.3 m/WiFeS	2014 Oct 7	1	3	54
ANU 2.3 m/WiFeS	2014 Oct 8–10	2	7	51–62	33.3	4000
Euler 1.2 m/Coralie	2014 Oct–2016 Jan	11	60	14–29	37.08	440
AAT 3.9 m/CYCLOPS2+UCLES	2015 Feb–May	8	70	13–17	38.00	375
ESO 3.6 m/HARPS	2015 Nov–2016 Mar	5	115	13–25	37.25	275
HATS-42						
ANU 2.3 m/WiFeS	2014 Jun 4	1	3	40
ANU 2.3 m/WiFeS	2014 Dec 11–12	2	7	34–46	7.4	4000
ESO 3.6 m/HARPS	2015 Apr–Nov	5	115	11–18	8.163	34
MPG 2.2 m/FEROS	2016 Jan 16–21	4	48	41–47	8.131	90

^a S/N per resolution element near 5180 Å.

^b For high-precision radial velocity observations included in the orbit determination this is the zero-point radial velocity from the best-fit orbit. For other instruments it is the mean value. We do not provide this quantity for the lower resolution WiFeS observations which were only used to measure stellar atmospheric parameters.

^c For high-precision radial velocity observations included in the orbit determination this is the scatter in the radial velocity residuals from the best-fit orbit (which may include astrophysical jitter), for other instruments this is either an estimate of the precision (not including jitter), or the measured standard deviation. We do not provide this quantity for low-resolution observations from the ANU 2.3 m/WiFeS.

dwarf. Two radial velocity measurements showed no significant variation, though they were both obtained near the same quadrature phase.

- HATS-41 has an effective temperature of $6327 \pm 300\text{K}$, $\log g_*$ of 3.9 ± 0.3 and metallicity of $[\text{Fe}/\text{H}] = 0.0 \pm 0.5$. We conclude that the target is an F dwarf. The two radial velocity measurements taken at either quadrature phase showed no significant variation.
- HATS-42 was measured to have an effective temperature of $6249 \pm 300\text{K}$, $\log g_*$ of 4.0 ± 0.3 and

metallicity of $[\text{Fe}/\text{H}] = 0.0 \pm 0.5$. Based on this we conclude that the target is a G- or F-dwarf. Two radial velocity measurements taken at either quadrature phase also showed no significant variation.

This initial vetting excluded these targets as giant host stars, and except for HATS-40, as eclipsing binaries, and thus all were then promoted to the next phase in the follow-up campaign, leading to further higher radial-velocity-precision spectroscopy and photometric follow-up. In the case of HATS-40 we began collecting higher precision RV observations before both quadrature

phases were covered by WiFeS, and it became clear from these data that this object is not an eclipsing binary, and further WiFeS observations were not needed.

2.2.2. High-precision spectroscopic observations

A full radial velocity characterisation covering a wide portion of the orbital phase of all of our targets is required in order to determine fundamental parameters such as the planetary masses and orbital eccentricities. As such, observations were performed with a range of facilities capable of high precision radial velocity measurements on single visits. Exposures were taken with the High Accuracy Radial Velocity Planet Searcher (Mayor et al. 2003, HARPS), fed by the ESO 3.6m telescope at a resolving power of $R \sim 115,000$, the FEROS spectrograph (Kaufer & Pasquini 1998, $R \sim 48,000$) fed by the MPG 2.2m telescope, and spectra at $R \sim 60,000$ were also taken with the CORALIE spectrograph (Queloz et al. 2001) fed by the 1.2m Euler telescope, all located at La Silla Observatory, Chile. The data reduction for all these spectra was performed us-

ing the method described in Jordán et al. (2014) and Brahm et al. (2017a). Additionally, eleven spectra of HATS-39 and HATS-41 were also obtained with the CYCLOPS2 fibre-feed and the UCLES spectrograph on the 3.9m Anglo-Australian telescope (AAT) at SSO at a resolving power of $R \sim 70,000$. These data were reduced using the methods described in Addison et al. (2013). Further details about these observations can be found in Table 2. The resulting data sets for all targets can be found in Table 3, and are shown in Figure 2, which includes radial velocity curves, best-fit models and bisector span (BS) (Queloz et al. 2001) estimates shown in the bottom panels for each target. All systems clearly show a radial velocity variation consistent with the detected transit ephemeris from the photometric light curves and no clear correlation between the radial velocity measurements and the bisector-spans, indicating the systems are likely bona fide transiting planets (see Section 3.2). We note that bisector span measurements from CYCLOPS2+UCLES are not available as the pipeline does not have the facility to measure these at this time.

Table 3. Relative radial velocities (RV) and bisector spans (BS) for HATS-39–HATS-42.

BJD (2,450,000+)	RV ^a (m s ⁻¹)	σ_{RV} ^b (m s ⁻¹)	BS ^c (m s ⁻¹)	σ_{BS} (m s ⁻¹)	Phase	Instrument
HATS-39						
7067.62167	-25.89	22.00	95.0	19.0	0.897	HARPS
7068.65140	-102.89	33.00	97.0	30.0	0.122	HARPS
7069.66662	-76.89	23.00	-2.0	21.0	0.344	HARPS
7070.67868	-22.89	20.00	7.0	17.0	0.565	HARPS
7071.64200	75.11	17.00	9.0	14.0	0.776	HARPS
7072.64113	13.11	26.00	9.0	21.0	0.994	HARPS
7083.02827	16.80	17.10	0.263	CYCLOPS
7083.04429	-140.40	16.80	0.267	CYCLOPS
7083.06038	-134.10	39.50	0.270	CYCLOPS
7118.58681	-8.89	22.00	-7.0	19.0	0.031	HARPS
7119.52550	3.11	25.00	-51.0	21.0	0.236	HARPS
7120.57144	10.11	33.00	146.0	26.0	0.464	HARPS
7329.85316	-106.89	35.00	37.0	26.0	0.183	HARPS
7331.84959	72.11	21.00	-49.0	17.0	0.619	HARPS
7331.86410	82.11	21.00	-28.0	17.0	0.622	HARPS
7332.83972	73.11	21.00	9.0	19.0	0.835	HARPS
7466.55350	29.11	32.00	16.0	21.0	0.045	HARPS
7467.54434	-33.89	18.00	-1.0	11.0	0.262	HARPS
7468.55331	2.11	18.00	-25.0	11.0	0.482	HARPS

Table 3 continued

Table 3 (continued)

BJD (2,450,000+)	RV ^a (m s ⁻¹)	σ_{RV} ^b (m s ⁻¹)	BS ^c (m s ⁻¹)	σ_{BS} (m s ⁻¹)	Phase	Instrument
7495.58378	-40.89	20.00	24.0	14.0	0.387	HARPS
HATS-40						
7067.56779	-78.13	44.00	0.133	HARPS
7069.58400	216.87	41.00	60.0	29.0	0.751	HARPS
7070.56482	-113.13	51.00	0.051	HARPS
7071.57968	-148.13	39.00	0.362	HARPS
7072.59059	127.87	58.00	0.672	HARPS
7118.55616	60.87	93.00	-420.0	94.0	0.753	HARPS
7119.49884	-51.13	48.00	59.0	34.0	0.042	HARPS
7120.49030	-109.13	36.00	-58.0	26.0	0.346	HARPS
7329.74873	-12.13	79.00	-298.0	47.0	0.452	HARPS
7332.77781	-66.13	38.00	-19.0	26.0	0.380	HARPS
HATS-41						
6939.87473	237.04	112.00	-404.0	21.0	0.373	Coralie
6969.82238	107.04	117.00	-399.0	22.0	0.515	Coralie
6971.81055	-693.96	146.00	-617.0	35.0	0.989	Coralie
7080.00880	666.54	118.60	0.789	CYCLOPS
7080.07261	431.24	223.90	0.804	CYCLOPS
7080.08861	1289.54	31.60	0.808	CYCLOPS
7082.92936	-171.56	90.80	0.486	CYCLOPS
7082.94532	26.94	59.80	0.489	CYCLOPS
7082.96128	157.44	74.90	0.493	CYCLOPS
7109.59087	-68.96	166.00	-654.0	32.0	0.843	Coralie
7150.86119	1139.44	111.50	0.684	CYCLOPS
7150.87728	985.24	87.40	0.688	CYCLOPS
7282.89965	-1104.96	117.00	-296.0	29.0	0.170	Coralie
7312.79578	-656.96	107.00	-166.0	26.0	0.299	Coralie
7318.75358	336.04	120.00	239.0	26.0	0.719	Coralie
7329.76516	-584.98	83.00	-121.0	49.0	0.345	HARPS
7331.78101	744.02	52.00	-238.0	26.0	0.826	HARPS
7332.79161	-1197.98	57.00	-72.0	31.0	0.067	HARPS
7408.60163	-1167.96	82.00	-44.0	22.0	0.144	Coralie
7409.56696	367.04	93.00	-679.0	25.0	0.374	Coralie
7410.69245	1233.04	79.00	-307.0	21.0	0.643	Coralie
7411.56574	912.04	137.00	-10178.0	26.0	0.851	Coralie
7467.50487	-918.98	69.00	-134.0	24.0	0.190	HARPS
7468.49670	426.02	81.00	11.0	28.0	0.426	HARPS
HATS-42						
7119.55661	-222.35	35.00	7.0	38.0	0.113	HARPS
7120.51754	49.65	20.00	-100.0	27.0	0.532	HARPS
7330.82381	-241.35	31.00	-20.0	38.0	0.285	HARPS
7331.76070	223.65	17.00	37.0	21.0	0.693	HARPS
7332.80517	-194.35	29.00	18.0	32.0	0.149	HARPS

Table 3 continued

Table 3 (continued)

BJD	RV ^a	σ_{RV} ^b	BS ^c	σ_{BS}	Phase	Instrument
(2,450,000+)	(m s ⁻¹)	(m s ⁻¹)	(m s ⁻¹)	(m s ⁻¹)		
7403.81476	-112.92	15.00	-1.0	15.0	0.129	FEROS
7404.83808	185.08	17.00	126.0	17.0	0.576	FEROS
7407.54463	113.08	16.00	-143.0	16.0	0.756	FEROS
7408.68903	-271.92	16.00	-80.0	15.0	0.256	FEROS

^a The zero-point of these velocities is arbitrary. An overall offset γ_{rel} fitted independently to the velocities from each instrument has been subtracted.

^b Internal errors excluding the component of astrophysical jitter considered in Section 3.3.

^c Bisector span measurements are only shown for observations in which the automated routines in the individual instrument pipelines were able to determine them. For cases where the peak of the cross-correlated function was too low to obtain a reliable measurement, these values are not presented.

2.3. Photometric follow-up observations

Photometric follow-up is also undertaken to both confirm the transit signal and improve light curves parameter estimates for each system. All four candidates were observed with the LCOGT network (Brown et al. 2013) – specifically using the 1m aperture telescopes of this network in the *i* band, which obtained several full- and partial-transits for HATS-39, HATS-40 and HATS-41. Additionally, a partial transit of HATS-40 was observed with the PEST 0.3m telescope in Western Australia in the *R_C* band. Full transits of HATS-39 and HATS-42, as well as a partial transit of HATS-41, were also observed with the Swope 1m telescope in Las Campanas, Chile in the *i* band. This data set includes a full transit of HATS-39 observed simultaneously with both Swope and LCOGT on Jan 9th 2016. The photometric data were acquired using the same strategy, and reduced using a customisable pipeline and the methods described in Penev et al. (2013), with details of setup in Bayliss et al. (2015). This pipeline uses standard photometric reduction frames (master bias, darks, twilight flats) and the DAOPHOT aperture photometry package for flux extraction of target and comparison stars. A quadratic trend in time, as well as variations correlated with point-spread-function shape, were fitted simultaneously with the transit shape to compensate for variable seeing and differential refraction. We assume an ellipsoidal Gaussian PSF parameterized by

$$e^{-\frac{1}{2}(S(x^2+y^2)+D(x^2-y^2)+K(2xy))}, \quad (1)$$

where the coefficients *S*, *D* and *K* are allowed to vary freely and can be mapped to FWHM, elongation and position angle. These photometric follow-up observations are summarized in Table 1, and all the resulting photometric data are available in electronic format in Table 4. The full set of photometric follow-up light curves are shown in Figures 3, 4, 5, and 6, for HATS-39, HATS-40,

HATS-41, and HATS-42, with the data plotted along with the best fit models and residuals plotted underneath.

2.4. Lucky Imaging

Lucky imaging observations were obtained through a *z'* filter for all four systems using the Astralux Sur camera (Hippler et al. 2009) on the New Technology Telescope (NTT) at La Silla Observatory in Chile on the night of 2015 December 22. Observations with this facility were carried out and reduced following Espinoza et al. (2016), but a plate scale of 15.20 mas pixel⁻¹ was used, derived in the work of Janson et al. (2017). Figure 7 shows the reduced final images for each system, while Figure 8 shows the 5 σ contrast curves based on these images produced using the technique and software described in Espinoza et al. (2016).

For HATS-39 we achieve an effective FWHM for the final image of 0''.0368 \pm 0''.0046, equivalent to 2.42 \pm 0.30 pixels. For this object a neighboring source is detected at 1''.32 \pm 0''.02 in Declination and 0''.68 \pm 0''.02 in RA (i.e., at a distance of 2''.2 from the target; errors on RA and DEC are obtained as the effective FWHM divided by 2.355) from the target at $\sim 2\sigma$ confidence. The apparent source, if real, has $\Delta z' = 5.65 \pm 0.35$ mag relative to HATS-39, and cannot be responsible for the transits. This candidate neighbour also has a negligible impact on the inferred parameters of the HATS-39b system.

For HATS-40 we obtained an effective FWHM of 2.92 \pm 0.35 pixels, or 0''.0444 \pm 0''.0053 and no companion sources were detected. Similarly, for HATS-41 we obtained an effective FWHM of 2.64 \pm 0.34 pixels, or 0''.0401 \pm 0''.0052 and no companions were detected.

In the case of HATS-42 (effective FWHM of 5.01 \pm 0.32 pixels, equivalent to 0''.0761 \pm 0''.0049) a nearby source is also detected at a $\sim 2\sigma$ level. The target is at -3''.56 \pm 0''.03 in Dec and -0''.93 \pm 0''.03 in RA (i.e.,

Table 4. Light curve data for HATS-39, HATS-40, HATS-41 and HATS-42.

Object ^a	BJD ^b	Mag ^c	σ_{Mag}	Mag(orig) ^d	Filter	Instrument
(2,400,000+)						
HATS-39	55939.70502	-0.01394	0.00416	...	<i>r</i>	HS/G602.3
HATS-39	55916.81716	-0.00641	0.00364	...	<i>r</i>	HS/G602.3
HATS-39	55948.86125	-0.00034	0.00414	...	<i>r</i>	HS/G602.3
HATS-39	55962.59487	-0.00385	0.00494	...	<i>r</i>	HS/G602.3
HATS-39	55880.19892	0.01622	0.00511	...	<i>r</i>	HS/G602.3
HATS-39	55971.75158	0.00319	0.00420	...	<i>r</i>	HS/G602.3
HATS-39	55843.57819	0.02082	0.00564	...	<i>r</i>	HS/G602.3
HATS-39	55939.70882	-0.02094	0.00429	...	<i>r</i>	HS/G602.3
HATS-39	55916.82201	0.00981	0.00372	...	<i>r</i>	HS/G602.3
HATS-39	55880.20276	0.01193	0.00527	...	<i>r</i>	HS/G602.3

^a Either HATS-39, HATS-40, HATS-41 or HATS-42.

^b Barycentric Julian Date is computed directly from the UTC time without correction for leap seconds.

^c The out-of-transit level has been subtracted. For observations made with the HATSouth instruments (identified by “HS” in the “Instrument” column) these magnitudes have been corrected for trends using the EPD and TFA procedures applied *prior* to fitting the transit model. This procedure may lead to an artificial dilution in the transit depths. The blend factors for the HATSouth light curves are listed in Table 6. For observations made with follow-up instruments (anything other than “HS” in the “Instrument” column), the magnitudes have been corrected for a quadratic trend in time, and for variations correlated with up to three PSF shape parameters, fit simultaneously with the transit.

^d Raw magnitude values without correction for the quadratic trend in time, or for trends correlated with the seeing. These are only reported for the follow-up observations.

NOTE— This table is available in a machine-readable form in the online journal. A portion is shown here for guidance regarding its form and content.

at a distance of $3''.68$ from the target). The magnitude difference for these two stars is 4.769 ± 0.052 . This nearby target is also detected by the Gaia space observatory (Lindgren et al. 2016) at a separation of $-3''.6187 \pm 0''.0003$ in Dec and $-0''.9104 \pm 0.0002$ in RA, numbers which are in perfect agreement with our values; they also find a magnitude difference in the *g* band of 3.553 magnitudes, confirming the existence of this target as real. This source is, however, not able to be responsible for the observed transits at this brightness.

3. ANALYSIS

3.1. Properties of the parent star

We used the Zonal Atmospheric Stellar Parameter Estimator (ZASPE; Brahm et al. 2017b) to model the stellar parameters of all four host stars. ZASPE is capable of precise stellar atmospheric parameter estimation from high-resolution echelle spectra of FGK-type stars. It compares the observed continuum-normalized spectrum with a grid of synthetic spectra by a least squares minimisation in the most sensitive regions of the stellar spectrum. The complete FGK-type star parameter space is searched using this method. To take into account

the microturbulence dependence of the line widths, we use an empirical relation between the microturbulence and the stellar parameters. In particular, we used the stellar parameters provided by the SweetCat catalogue (Santos et al. 2013) define a polynomial that delivers the microturbulence as function of effective temperature and $\log g$. Then, the microturbulence value used in the synthesis of each spectrum was obtained using that empirical function. More details on this method can be found in Brahm et al. (2017b). We performed this analysis on the combined HARPS spectra for HATS-39, HATS-40 and HATS-41, and on the FEROS spectra for HATS-42.

We calculate an initial estimate of the effective temperature (T_{eff}), the surface gravity ($\log g$), metallicity ($[\text{Fe}/\text{H}]$) and projected stellar rotational velocity of the stars ($v \sin i$). Following Sozzetti et al. (2007), we used the stellar density ρ_* , which was determined from the modeling described in Section 3.3, together with T_{eff} and $[\text{Fe}/\text{H}]$ to determine the other physical parameters of the host star through a comparison with the Yonsei-Yale (Y2; Yi et al. 2001) isochrones. If the value of $\log g_*$ from the stellar evolution modeling is discrepant from

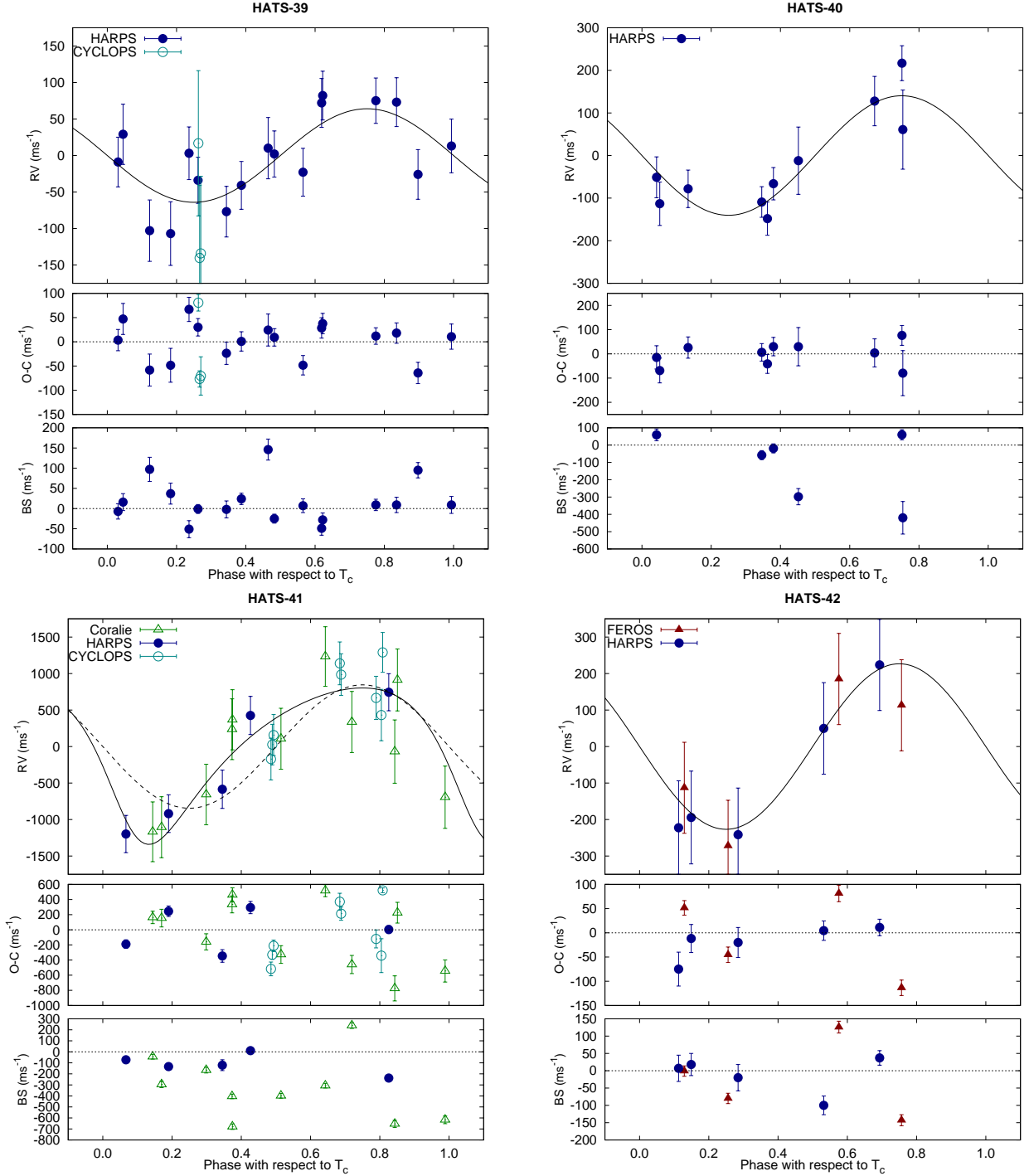


Figure 2. Phased high-precision radial velocity measurements for HATS-39 (upper left), HATS-40 (upper right), HATS-41 (lower left) and HATS-42 (lower right). The instruments used are labeled in the plots. In each case we show three panels. The top panel shows the phased measurements together with our best-fit model (see Table 6) for each system. Zero-phase corresponds to the time of mid-transit. The center-of-mass velocity has been subtracted. The second panel shows the velocity $O-C$ residuals from the best fit. The error bars in the middle panel correspond to the formal uncertainties only and, on the top panel, we show final uncertainties with the jitter terms listed in Table 6 added in quadrature. The third panel shows the bisector spans (BS). Note the different vertical scales of the panels. We include the zero eccentricity model fit for the case of HATS-41 for reference.

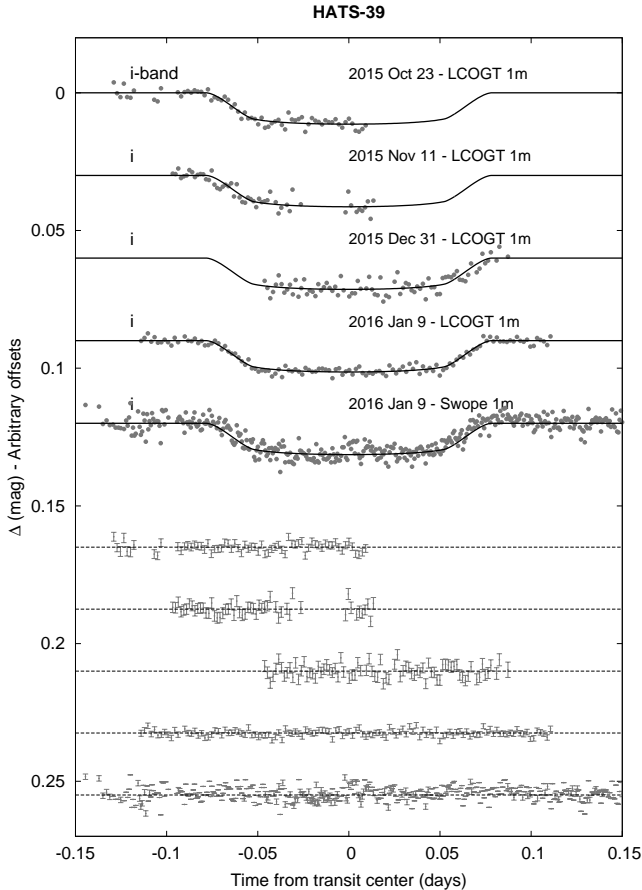


Figure 3. Unbinned transit light curves for HATS-39. The light curves have been corrected for quadratic trends in time, and linear trends with up to three parameters characterizing the shape of the PSF, fitted simultaneously with the transit model. The dates of the events, filters and instruments used are indicated. Light curves following the first are displaced vertically for clarity. Our best fit from the global modeling described in Section 3.3 is shown by the solid lines. The residuals from the best-fit model are shown below in the same order as the original light curves. The error bars represent the photon and background shot noise, plus the readout noise.

the value determined in the initial ZASPE analysis of the spectrum by more than 1σ , we perform a second iteration of ZASPE using $\log g_*$ determined from the isochrones, followed by a second iteration of the analysis in Section 3.3 and comparison to the Y2 isochrones. This was done to improve the results for HATS-39 and HATS-42. The second iteration was not needed for the other two candidates. We present the adopted results and an extensive set of host star parameters from several sources in Table 5.

All host stars were found to be F-type dwarf stars. We find HATS-39 to be a solar metallicity star with $T_{\text{eff}} = 6572 \pm 83$ K, mass $M_* = 1.374^{+0.075}_{-0.057} M_{\odot}$ and ra-

dius $R_* = 1.59 \pm 0.25 R_{\odot}$. HATS-40 is also solar metallicity, but more massive and larger ($M_* = 1.58 \pm 0.11 M_{\odot}$ and $R_* = 2.33^{+0.37}_{-0.22} R_{\odot}$). HATS-41 and HATS-42 have metallicities above the solar one with $[\text{Fe}/\text{H}] = 0.470 \pm 0.041$ and $[\text{Fe}/\text{H}] = 0.220 \pm 0.070$ (respectively). Both stars are also somewhat above solar mass, and have similar radii. We refer the reader to Table 5 for further details.

Distances to these stars were determined by comparing the measured broad-band photometry listed in Table 5 to the predicted magnitudes in each filter from the isochrones. We assumed a $R_V = 3.1$ extinction law from Cardelli et al. (1989) to determine the extinction and find these to be consistent within their uncertainties to reddening maps available on the NASA/IPAC infrared science archive². The locations of each star on an $T_{\text{eff}*}-\rho_*$ diagram (similar to a Hertzsprung-Russell diagram) are shown in Figure 9.

3.2. Excluding blend scenarios

In order to exclude blend scenarios we carried out an analysis following Hartman et al. (2012). We attempt to model the available photometric data (including light curves and catalog broad-band photometric measurements) for each object as a blend between an eclipsing binary star system and a third star along the line of sight. The physical properties of the stars are constrained using the Padova isochrones (Girardi et al. 2000), while we also require that the brightest of the three stars in the blend have atmospheric parameters consistent with those measured with ZASPE. We also simulate composite cross-correlation functions and use them to predict radial velocities and bisector spans for each blend scenario considered. The results for each system are as follows:

- *HATS-39* – all blend scenarios tested give a poorer fit to the photometric data than a model consisting of a single star with a planet, though for the best-fit blend models the difference in χ^2 compared to the best-fit planet model is not statistically significant. The simulated bisector spans and radial velocities for all blend models that cannot be ruled out by the photometry (i.e., those that cannot be rejected with greater than 5σ confidence) show variations in excess of 100 m s^{-1} , and in most cases in excess of 1 km s^{-1} . This contrasts with the measured HARPS velocities which have a sinusoidal variation with an amplitude of $K = 62 \pm 13 \text{ m s}^{-1}$,

² Publicly available at <http://irsa.ipac.caltech.edu/applications/DUST/>

Table 5. Stellar parameters for HATS-39–HATS-42

Parameter	HATS-39 Value	HATS-40 Value	HATS-41 Value	HATS-42 Value	Source
Astrometric properties and cross-identifications					
2MASS-ID	07294061-2956163	06421710-2946365	06540416-2703013	07134857-3326143	
GSC-ID	GSC 6550-00341	GSC 6533-01514	GSC 6530-01596	GSC 7107-03973	
R.A. (J2000)	07 ^h 29 ^m 40.63s	06 ^h 42 ^m 17.10s	06 ^h 54 ^m 04.18s	07 ^h 13 ^m 48.58s	2MASS
Dec. (J2000)	−29°56′16.4″	−29°46′36.5″	−27°03′01.4″	−33°26′14.4″	2MASS
$\mu_{R.A.}$ (mas yr ^{−1})	−0.2 ± 1.0	−4.6 ± 2.1	0.60 ± 0.90	0.9 ± 1.3	UCAC4
$\mu_{Dec.}$ (mas yr ^{−1})	−5.9 ± 1.7	5.6 ± 2.3	−7.0 ± 1.0	1.7 ± 1.3	UCAC4
Spectroscopic properties					
$T_{\text{eff}\star}$ (K)	6572 ± 83	6460 ± 130	6424 ± 91	6060 ± 120	ZASPE ^a
[Fe/H]	0.000 ± 0.044	0.010 ± 0.077	0.470 ± 0.041	0.220 ± 0.070	ZASPE
$v \sin i$ (km s ^{−1})	7.75 ± 0.17	9.52 ± 0.25	19.21 ± 0.23	6.04 ± 0.36	ZASPE
v_{mac} (km s ^{−1})	5.21 ± 0.13	5.04 ± 0.20	4.99 ± 0.14	4.42 ± 0.19	Assumed
v_{mic} (km s ^{−1})	1.86 ± 0.12	1.70 ± 0.17	1.66 ± 0.12	1.28 ± 0.10	Assumed
γ_{RV} (m s ^{−1})	2916.2 ± 8.7	9194 ± 17	37250 ± 220	8163 ± 13	HARPS ^b
Photometric properties					
G (mag)	12.58	13.22	12.52	13.48	GAIA DR1 ^c
B (mag)	13.232 ± 0.010	13.866 ± 0.020	13.175 ± 0.040	14.243 ± 0.010	APASS ^d
V (mag)	12.746 ± 0.020	13.377 ± 0.030	12.681 ± 0.030	13.617 ± 0.010	APASS ^d
g (mag)	12.907 ± 0.020	13.557 ± 0.020	12.893 ± 0.040	13.922 ± 0.050	APASS ^d
r (mag)	12.578 ± 0.050	13.272 ± 0.040	12.555 ± 0.020	13.498 ± 0.010	APASS ^d
i (mag)	12.542 ± 0.060	13.197 ± 0.040	12.484 ± 0.060	13.396 ± 0.050	APASS ^d
J (mag)	11.833 ± 0.024	12.439 ± 0.026	11.765 ± 0.024	12.543 ± 0.024	2MASS
H (mag)	11.620 ± 0.024	12.242 ± 0.032	11.521 ± 0.023	12.281 ± 0.026	2MASS
K_s (mag)	11.518 ± 0.023	12.147 ± 0.027	11.498 ± 0.023	12.245 ± 0.029	2MASS
Derived properties					
M_\star (M_\odot)	1.379 ± 0.040	1.561 ± 0.069	1.496 ^{+0.115} _{−0.078}	1.273 ± 0.067	YY+ ρ_\star +ZASPE ^e
R_\star (R_\odot)	1.621 ± 0.085	2.26 ^{+0.18} _{−0.11}	1.71 ^{+0.36} _{−0.24}	1.48 ^{+0.20} _{−0.12}	YY+ ρ_\star +ZASPE
$\log g_\star$ (cgs)	4.158 ± 0.038	3.921 ± 0.041	4.14 ± 0.11	4.201 ± 0.070	YY+ ρ_\star +ZASPE
ρ_\star (g cm ^{−3}) ^f	0.458 ^{+0.076} _{−0.057}	0.190 ± 0.027	0.48 ^{+0.37} _{−0.20}	0.56 ± 0.13	Light curves
ρ_\star (g cm ^{−3}) ^f	0.457 ^{+0.075} _{−0.056}	0.189 ± 0.027	0.42 ± 0.17	0.55 ± 0.13	YY+Light curves+ZASPE
L_\star (L_\odot)	4.37 ± 0.53	8.0 ^{+1.5} _{−1.1}	4.5 ^{+2.1} _{−1.2}	2.66 ^{+0.77} _{−0.47}	YY+ ρ_\star +ZASPE
M_V (mag)	3.13 ± 0.14	2.47 ± 0.18	3.08 ± 0.37	3.71 ± 0.25	YY+ ρ_\star +ZASPE
M_K (mag,ESO)	2.12 ± 0.12	1.41 ± 0.14	2.00 ± 0.35	2.37 ± 0.22	YY+ ρ_\star +ZASPE
Age (Gyr)	2.06 ± 0.30	2.07 ± 0.34	1.34 ^{+0.31} _{−0.51}	3.26 ± 0.83	YY+ ρ_\star +ZASPE
A_V (mag)	0.186 ± 0.069	0.120 ± 0.096	0.081 ± 0.073	0.000 ± 0.065	YY+ ρ_\star +ZASPE
Distance (pc)	773 ± 41	1431 ⁺¹¹⁶ _{−75}	800 ⁺¹⁷⁰ _{−110}	942 ⁺¹²⁶ _{−80}	YY+ ρ_\star +ZASPE

NOTE— For HATS-41b we adopt a model in which the eccentricity is allowed to vary. For the other three systems we adopt a model in which the orbit is assumed to be circular. See the discussion in Section 3.3.

^a ZASPE = Zonal Atmospheric Stellar Parameter Estimator routine for the analysis of high-resolution spectra (Brahm et al. 2017b), applied to the HARPS spectra of HATS-39, HATS-40, and HATS-41, and to the FEROS spectra of HATS-42. These parameters rely primarily on ZASPE, but have a small dependence also on the iterative analysis incorporating the isochrone search and global modelling of the data.

^b The error on γ_{RV} is determined from the orbital fit to the radial velocity measurements, and does not include the systematic uncertainty in transforming the velocities to the IAU standard system. The velocities have not been corrected for gravitational redshifts.

^c From GAIA Data Release 1 (Lindegren et al. 2016). HATS-39 has a neighbour detected 4.35″ away with a magnitude of $G = 18.27$ ($\Delta G = 5.69$). HATS-42 has a detected nearby source at 3.61″ distance and with $G = 17.04$ ($\Delta G = 3.56$).

^d From APASS DR6 (Henden & Munari 2014) for as listed in the UCAC 4 catalog (Zacharias et al. 2012).

^e YY+ ρ_\star +ZASPE = Based on the YY isochrones (Yi et al. 2001), ρ_\star as a luminosity indicator, and the ZASPE results.

^f In the case of ρ_\star we list two values. The first value is determined from the global fit to the light curves and radial velocity data, without imposing a constraint that the parameters match the stellar evolution models. The second value results from restricting the posterior distribution to combinations of $\rho_\star + T_{\text{eff}\star} + [\text{Fe}/\text{H}]$ that match to a YY stellar model.

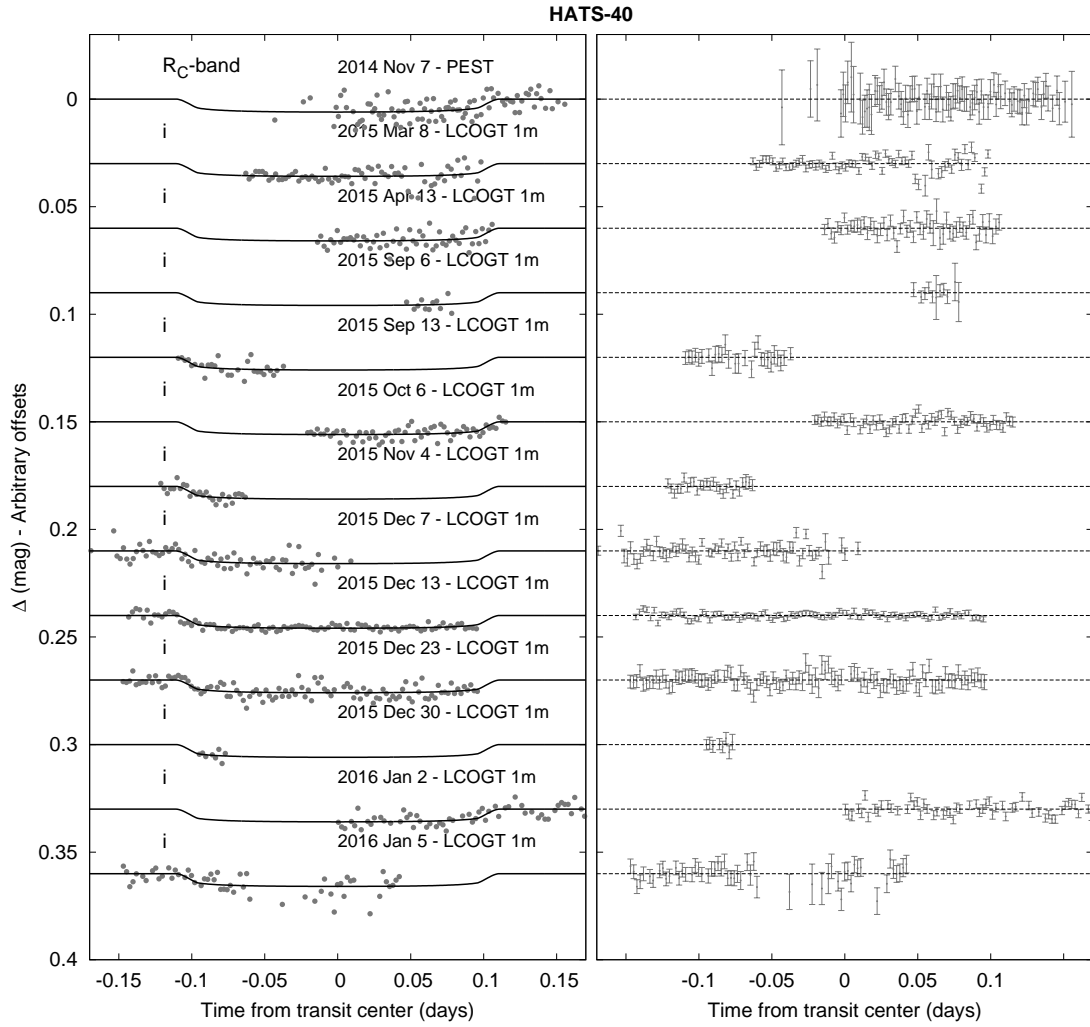


Figure 4. Similar to Fig. 3, here we show light curves for HATS-40. In this case the residuals are plotted on the right-hand-side of the figure, in the same order as the original light curves on the left-hand-side.

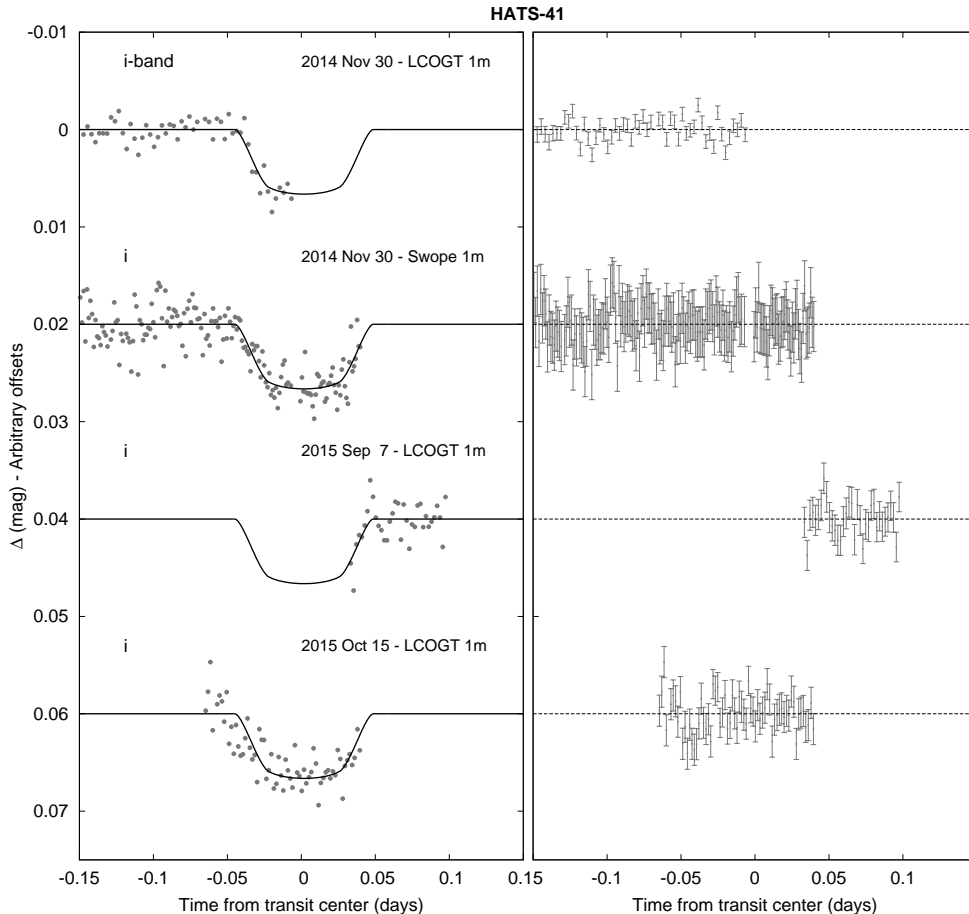


Figure 5. Same as Fig. 4, here we show light curves for HATS-41.

and a standard deviation (not subtracting the Keplerian orbit) of 59 m s^{-1} . Likewise the measured HARPS bisector spans have a standard deviation of 52 m s^{-1} , which is significantly less than the simulated values for all blend models that cannot be ruled out by the photometry. Based on this, we reject the hypothesis that HATS-39 is a blended stellar eclipsing binary object rather than a transiting planet system.

- *HATS-40* – in this case we find that all blend scenarios tested provide a much poorer fit to the photometric data than a single star with a planet. In fact, all blend models can be rejected with a confidence greater than 4.6σ , based on the photometry alone. We conclude that HATS-40 is not a blended stellar eclipsing binary object, but is a transiting planet system.
- *HATS-41* – there exist blend models that provide slightly better fits to the photometric data than a single star with a planet. We find that the best-fit blend model (a hierarchical triple system with a bright third star having $M_3 = 1.453 M_\odot$,

and an eclipsing binary with $M_1 = 1.05 M_\odot$, and $M_2 = 0.28 M_\odot$) has a value of χ^2 (based on all of the photometric data) that is 7.6 less than the value of χ^2 for the best-fit model consisting of a single star with a planet. Based on Monte Carlo simulations of photometric data with pink noise properties comparable to what is observed in the light curves, this corresponds to a 1.5σ confidence difference, and is thus not a large enough difference to be statistically significant. However, we find that none of the blend models that provide a reasonable fit to the photometric data are able to simultaneously reproduce both the observed radial velocity variation with $K = 820 \pm 170 \text{ m s}^{-1}$, and the measured 91 m s^{-1} scatter in the HARPS bisector span values. In general the simulated bisector span values have a correlated variation that is comparable in amplitude to the simulated radial velocity values. Blend scenarios that produce radial velocity variations at an amplitude above 1 km s^{-1} , also result in large BS variations at amplitude above 1 km s^{-1} , while blend scenarios that produce simulated BS variations with an ampli-

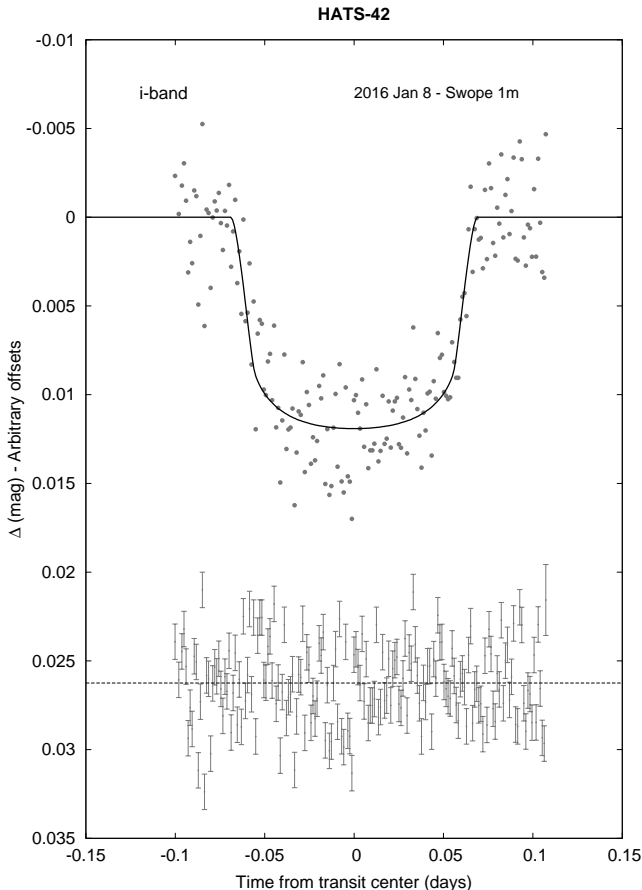


Figure 6. Same as Fig. 5, here we show light curve for HATS-42.

tude below 100 m s^{-1} , produce similarly low amplitude radial velocity variations. We conclude that blend scenarios cannot account for all of the photometric and spectroscopic observations of HATS-41, and furthermore conclude that HATS-41 is a transiting planet system.

- *HATS-42* – like HATS-40, all blend models tested can be rejected with a confidence greater than 4σ , based solely on the photometry. We conclude that HATS-42 is a transiting planet system, and not a blended stellar eclipsing binary object.

3.3. Global modeling of the data

We modeled the full available data for each target (initial photometry, follow-up photometry and spectroscopy) following the same method described in previous discoveries Pál et al. (2008); Bakos et al. (2010); Hartman et al. (2012). We fit Mandel & Agol (2002) transit models to all light curves, allowing for the possible dilution of the HATSouth transit depths as a result of blending from neighboring stars and over-correction

by the trend-filtering method. To correct for systematic errors in the follow-up light curves, such as airmass and pointing errors, we include in our model for each event a quadratic trend in time, and linear trends with up to three parameters describing the shape of the PSF. This ensures that seeing changes and centroiding errors are minimised. We then fit Keplerian orbits to the radial velocity curves allowing the zero-point for each instrument to vary independently in the fit, and allowing for radial velocity jitter, which is also allowed to vary for each instrument. A Differential Evolution Markov Chain Monte Carlo procedure is then performed to explore the fitness landscape and to determine the posterior distribution of the parameters.

Note that we tried fitting both fixed circular orbits and free-eccentricity models to the data for all 4 systems, and then use the method of Weinberg et al. (2013) to estimate the Bayesian evidence for each scenario. We find eccentricities consistent with zero for HATS-39, HATS-40 and HATS-42, in which the Bayesian evidence for the fixed circular orbit models are higher. For these three systems we adopt the parameters from the fixed circular orbit model solutions. For HATS-41 the free eccentricity model yields a marginally significant eccentricity of $e = 0.38 \pm 0.11$, with $\Delta\chi^2 = -14$ between the best-fit free eccentricity model, and the best-fit fixed circular orbit model. The Bayesian evidence for the fixed circular model is slightly higher by a factor of 6.7, but the best-fit circular orbit model yields a stellar density of $1.10^{+0.85}_{-0.34} \text{ g cm}^{-3}$, which is higher than allowed by the stellar evolution models at $T_{\text{eff}\star} = 6424 \pm 91 \text{ K}$. The free eccentricity model, on the other hand, yields a stellar density that falls within the range allowed by the stellar evolution models. For HATS-41 we adopt the parameters from a model where the eccentricity is allowed to vary in the fit, and include the zero eccentricity radial velocity solution in figure 2 for comparison. The high planet-to-star mass ratio leads to an estimate of 0.5 – 1.5 Gyr for a tidal circularisation timescale assuming present orbital characteristics and depending on assumptions on the quality factor Q_P between $1 - 3 \times 10^5$, typical values assumed for Jovian and dense Jovian planets (Pont et al. 2011). This value is consistent with the determined age for this system, and therefore some eccentricity is not unexpected.

The resulting parameters for each system are listed in Table 6.

4. DISCUSSION

We report the discovery of four transiting hot Jupiters orbiting F-type stars by the HATSouth survey: HATS-39b, HATS-40b, HATS-41b and HATS-42b. Among

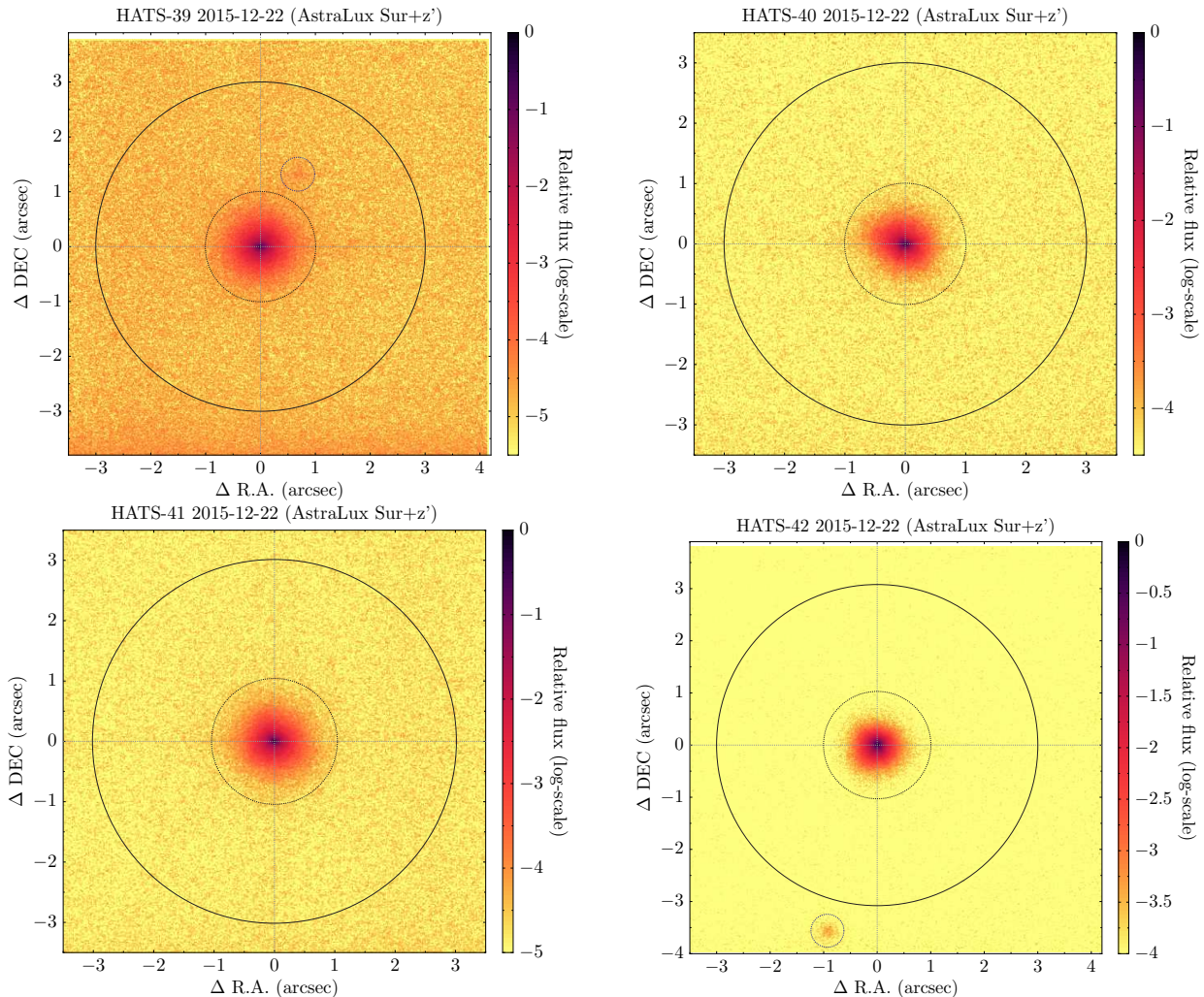


Figure 7. Astralux lucky images of HATS-39 (*top left*), HATS-40 (*top right*), HATS-41 (*bottom left*), and HATS-42 (*bottom right*). A neighboring source to HATS-39, indicated with a red circle, is detected at 2σ confidence at a separation of $\sim 2''$ in Declination and $\sim -1''$ in Right Ascension. If real, it has $\Delta z' = 5.65 \pm 0.35$ mag relative to HATS-39. No neighboring sources are detected in the observations of HATS-40, or HATS-41. HATS-42 has a real companion at $\sim -3.5''$ in Declination and $\sim -1''$ in Right Ascension also detected by the Gaia space observatory, but too faint to affect our results.

these is the particularly interesting case of HATS-41b which is one of the most massive hot Jupiters found to date and orbits the highest metallicity star to host a transiting planet, making it particularly important in the context of exoplanet discoveries to date. These add to the growing number of well-characterised exoplanets and provide further evidence of the diversity of these exotic worlds.

In Figure 10 we show these discoveries in the context of all other known hot Jupiters, which we define as planets with masses higher than $0.5M_J$ and orbital periods less than 10 days³.

In addition to previously known planets, we plot a selection of predicted mass–radius relations from Fortney et al. (2007) relevant for each of our planets. We have selected models for planets orbiting solar twins at 1 Gyr and 4.5 Gyr at a separation of 0.045 AU, and we plot two extreme values of the core masses – $0M_{\oplus}$ (solid lines) and $100M_{\oplus}$ (dashed lines). While the orbital distances of our new planets are mostly consistent with 0.045 AU, the nature of the host stars leads to a higher equilibrium temperature. Hence, we also show models for orbital separations of 0.02 AU, which correspond to an equilibrium temperature of 1960 K, more

³ Previously known planets shown in Figures 10 and 11 taken from the NASA Exoplanet Archive at

<http://exoplanetarchive.ipac.caltech.edu/> (Akeson et al. 2013)

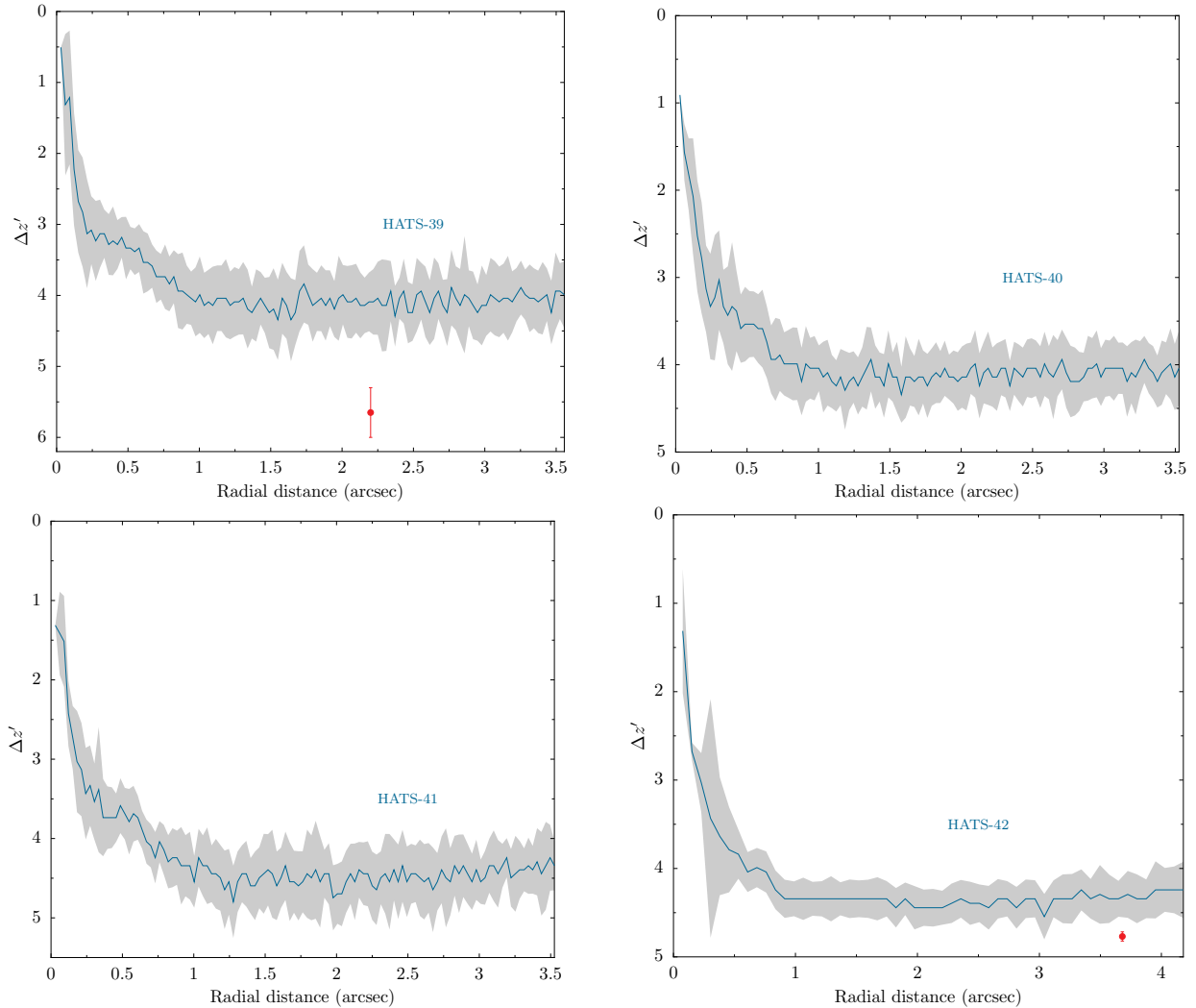


Figure 8. 5σ contrast curves for HATS-39 (*upper left*), HATS-40 (*upper right*), HATS-41 (*lower left*) and HATS-42 (*lower right*) based on our AstraLux Sur z' – band observations. The candidate neighboring source to HATS-39 detected with 2σ confidence is indicated by the filled circle and errorbar, and the same is done for the companion of HATS-42. Additional details on these companions can be found in the main text and on the footnotes of Table 5. Gray bands show the uncertainty given by the scatter in the contrast in the azimuthal direction at a given radius.

closely matching that of the four highlighted targets. While it is premature to make statements regarding the composition of these planets, HATS-39b and HATS-40b seem to be inflated with respect to these predicted models. In particular, HATS-39b is likely to be a good candidate for future transmission spectroscopy follow-up studies. Assuming a mean molecular mass similar to that of Jupiter, the scale height for this planets is approximately 970 km, which corresponds to a transmission signal during transit of 170 p.p.m. For a star of this magnitude ($J = 11.833 \pm 0.024$) this signal is expected to fall within the detection limits of JWST and would result in a more than 3σ detection (Pepe et al. 2014).

Of particular note is the case of HATS-41b. This very high mass planet is found to orbit the highest metallicity star to host a transiting planet to date. While there is a known relation between the stellar metallicity and giant planet frequency for low mass stars (Santos et al. 2004; Fischer & Valenti 2005), the recent work by Santos et al. (2017) suggests that perhaps there are, in fact, two distinct planet populations represented by those with masses above and below $\approx 4M_J$. The majority of higher mass planets are also found around higher mass (and sometimes evolved) host stars. The authors explore this in further detail and conclude that the dependence on host star metallicity found for lower mass planets is not present in those planets with masses higher than $4M_J$. Further-

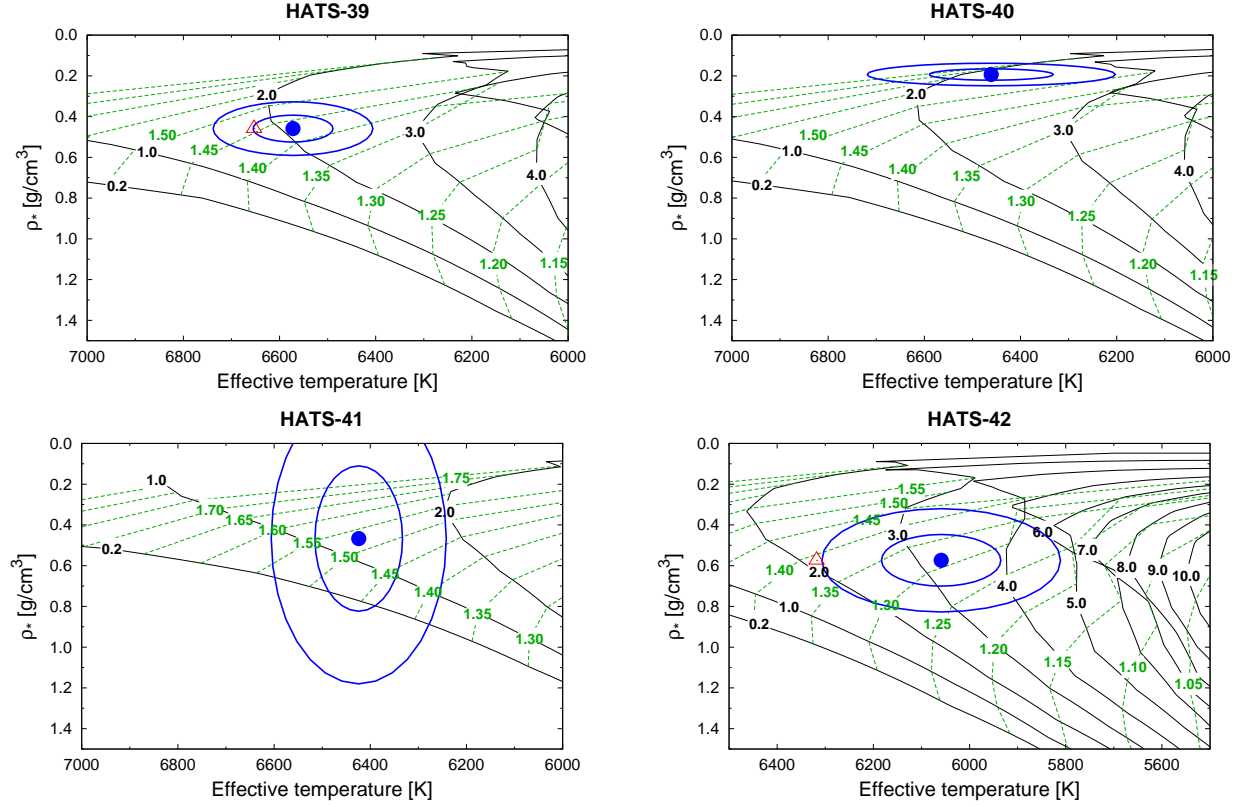


Figure 9. Plots of stellar density ρ_* as a function of effective temperature $T_{\text{eff}*}$ for the four new exoplanet discoveries. Model isochrones from Yi et al. (2001) for the measured metallicities of HATS-39 (upper left), HATS-40 (upper right), HATS-41 (lower left) and HATS-42 (lower right) are also shown as the black solid lines. These models have been chosen for a starting age of 0.2 Gyr, and then a range from 1.0 to 14.0 Gyr in 1 Gyr increments (ages increasing from left to right). We also plot in green dashed lines the evolutionary tracks for stars with masses listed in Solar units. The adopted values of $T_{\text{eff}*}$ and ρ_* are shown in the filled circle together with their 1σ and 2σ confidence ellipsoids. The initial values of $T_{\text{eff}*}$ and ρ_* from the first ZASPE and light curve analyses of HATS-39 and HATS-42 are represented with open triangles. The other two candidates did not require a second iteration.

more, on average, high mass giant planets are found orbiting hosts with slightly lower metallicity than their lower mass counterparts and therefore consistent with the metallicity distribution of average field stars with similar masses. These factors could be interpreted as these two populations of planets forming by different mechanisms, where lower mass planets are formed via a

core-accretion process (Perri & Cameron 1974; Mizuno 1980; Kennedy & Kenyon 2008) and the higher mass planets via another process where disk instability plays a role, as proposed by Cameron (1978); Boss (1998) and later revised by Rafikov (2005) and Nayakshin (2017).

Table 6. Orbital and planetary parameters for HATS-39b–HATS-42b

Parameter	HATS-39b Value	HATS-40b Value	HATS-41b Value	HATS-42b Value
Light curve parameters				
P (days)	4.5776348 ± 0.0000073	3.2642736 ± 0.0000058	4.193649 ± 0.000013	2.2921020 ± 0.0000021
T_c (BJD) ^a	$2457315.28338 \pm 0.00055$	2456962.6760 ± 0.0010	2456795.7240 ± 0.0014	$2456768.60734 \pm 0.00069$
T_{14} (days) ^a	0.1555 ± 0.0029	0.2221 ± 0.0031	0.0915 ± 0.0044	0.1361 ± 0.0032
$T_{12} = T_{34}$ (days) ^a	0.0256 ± 0.0029	0.0167 ± 0.0023	0.0215 ± 0.0065	0.0149 ± 0.0036

Table 6 continued

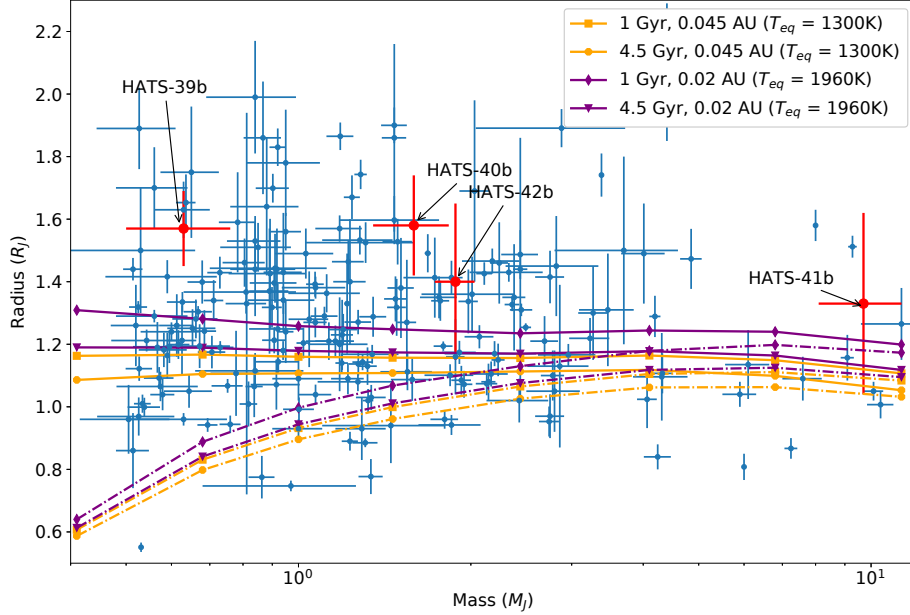


Figure 10. Mass-radius relation for hot Jupiters, defined as those planets with masses higher than $0.5M_J$ and periods shorter than 10 days. We show theoretical models for planet structures from [Fortney et al. \(2007\)](#) for both no core (dashed lines) and $100M_{\oplus}$ core (solid lines) scenarios. The new HATSouth planets are indicated. We present models at 1 Gyr and 4.5 Gyr for planets at a separation of 0.045 AU (orange lines), consistent with the separations of our new discoveries, and models at a separation of 0.02 AU that predict an equilibrium surface temperature of 1960K, closer to that of the four HATSouth targets. A colour version of this plot is available in the online version of this article.

Table 6 (*continued*)

Parameter	HATS-39b	HATS-40b	HATS-41b	HATS-42b
	Value	Value	Value	Value
a/R_*	7.97 ± 0.38	$4.74^{+0.22}_{-0.31}$	7.31 ± 0.98	$5.36^{+0.39}_{-0.56}$
ζ/R_* ^b	15.25 ± 0.14	9.738 ± 0.100	27.55 ± 0.89	16.51 ± 0.20
R_p/R_*	0.0993 ± 0.0029	0.0716 ± 0.0034	0.0798 ± 0.0036	0.0976 ± 0.0040
b^2	$0.485^{+0.042}_{-0.054}$	$0.122^{+0.104}_{-0.087}$	$0.721^{+0.050}_{-0.084}$	$0.21^{+0.16}_{-0.13}$
$b \equiv a \cos i/R_*$	$0.696^{+0.030}_{-0.040}$	$0.35^{+0.13}_{-0.16}$	$0.849^{+0.029}_{-0.051}$	$0.46^{+0.15}_{-0.18}$
i (deg)	84.98 ± 0.49	85.8 ± 1.8	$80.4^{+2.3}_{-4.2}$	85.1 ± 2.1
HATSouth dilution factors ^c				
Dilution factor 1	0.911 ± 0.058	0.888 ± 0.078	0.856 ± 0.090	0.928 ± 0.058
Dilution factor 2	0.782 ± 0.077	0.545 ± 0.087	...	0.885 ± 0.064
Dilution factor 3	0.83 ± 0.14
Limb-darkening coefficients ^d				
$c_{1,r}$	0.2375	0.2457	0.2634	0.3138
$c_{2,r}$	0.3875	0.3857	0.3954	0.3565
$c_{1,R}$	0.2393	...
$c_{2,R}$	0.3976	...
$c_{1,i}$	0.1654	0.1695	0.1795	0.2292
$c_{2,i}$	0.3772	0.3788	0.3965	0.3581

Table 6 continued

Table 6 (continued)

Parameter	HATS-39b Value	HATS-40b Value	HATS-41b Value	HATS-42b Value
Radial Velocity parameters				
K (m s ⁻¹)	62 ± 13	162 ± 23	1080 ± 190	246 ± 17
e^e	< 0.275	< 0.312	0.38 ± 0.11	< 0.229
ω (deg)	136 ± 18	...
$\sqrt{e} \cos \omega$	-0.43 ± 0.12	...
$\sqrt{e} \sin \omega$	0.42 ± 0.16	...
jitter HARPS (m s ⁻¹)	26 ± 12	< 33.7	350 ± 210	< 20.6
jitter FEROS (m s ⁻¹) ^f	100 ± 90
jitter CYCLOPS (m s ⁻¹)	< 312.8	...	380 ± 140	...
jitter Coralie (m s ⁻¹)	460 ± 150	...
Planetary parameters				
M_p (M_J)	0.63 ± 0.13	1.59 ± 0.24	9.7 ± 1.6	1.88 ± 0.15
R_p (R_J)	1.57 ± 0.12	1.58 ^{+0.16} _{-0.12}	1.33 ^{+0.29} _{-0.20}	1.40 ^{+0.25} _{-0.14}
$C(M_p, R_p)^g$	0.05	0.20	0.10	0.39
ρ_p (g cm ⁻³)	0.202 ^{+0.072} _{-0.051}	0.49 ± 0.13	5.1 ^{+3.3} _{-2.3}	0.83 ± 0.28
$\log g_p$ (cgs)	2.81 ± 0.12	3.191 ± 0.091	4.13 ± 0.16	3.369 ^{+0.092} _{-0.137}
a (AU)	0.06007 ± 0.00058	0.04997 ± 0.00074	0.0583 ^{+0.0015} _{-0.0010}	0.03689 ± 0.00065
T_{eq} (K)	1645 ± 43	2101 ± 69	1710 ⁺¹⁷⁰ ₋₁₂₀	1856 ⁺¹⁰⁵ ₋₇₆
Θ^h	0.0351 ± 0.0079	0.063 ± 0.010	0.60 ± 0.14	0.076 ± 0.011
$\log_{10}\langle F \rangle$ (cgs) ⁱ	9.218 ± 0.046	9.643 ± 0.057	9.29 ± 0.14	9.427 ^{+0.096} _{-0.073}

NOTE— For HATS-41b we adopt a model in which the eccentricity is allowed to vary. For the other three systems we adopt a model in which the orbit is assumed to be circular. See the discussion in Section 3.3.

^a Times are in Barycentric Julian Date calculated directly from UTC *without* correction for leap seconds. T_c : Reference epoch of mid transit that minimizes the correlation with the orbital period. T_{12} : total transit duration, time between first to last contact; $T_{12} = T_{34}$: ingress/egress time, time between first and second, or third and fourth contact.

^b Reciprocal of the half duration of the transit used as a jump parameter in our MCMC analysis in place of a/R_* . It is related to a/R_* by the expression $\zeta/R_* = a/R_*(2\pi(1 + e \sin \omega))/(P\sqrt{1 - b^2}\sqrt{1 - e^2})$ (Bakos et al. 2010).

^c Scaling factor applied to the model transit that is fit to the HATSouth light curves. This factor accounts for dilution of the transit due to blending from neighboring stars and over-filtering of the light curve. These factors are varied in the fit, with independent values adopted for each HATSouth light curve. The factors listed for HATS-39 are for the G602.3 and G602.4 light curves, respectively. For HATS-40, we list the factors for G601.2, G600.3, and G600.4, respectively. For HATS-41 the listed factor is for G601.2. For HATS-42, the listed factors are for G602.1 and G601.4, respectively.

^d Values for a quadratic law, adopted from the tabulations by Claret (2004) according to the spectroscopic (ZASPE) parameters listed in Table 5.

^e For HATS-39, HATS-40 and HATS-42 we list the 95% confidence upper limit on the eccentricity determined when $\sqrt{e} \cos \omega$ and $\sqrt{e} \sin \omega$ are allowed to vary in the fit.

^f Term added in quadrature to the formal radial velocity uncertainties for each instrument. This is treated as a free parameter in the fitting routine. In cases where the jitter is consistent with zero, we list its 95% confidence upper limit.

^g Correlation coefficient between the planetary mass M_p and radius R_p estimated from the posterior parameter distribution.

^h The Safronov number is given by $\Theta = \frac{1}{2}(V_{\text{esc}}/V_{\text{orb}})^2 = (a/R_p)(M_p/M_*)$ (see Hansen & Barman 2007).

ⁱ Incoming flux per unit surface area, averaged over the orbit.

While the authors focus on a sample of planets with orbital periods above 10 days to deliberately reject hot Jupiters, they note that their conclusion regarding the potential existence of two separate populations still stands if those planets are included, and therefore we can place our new discoveries in this context. In Figure 11 we show a plot of planet mass as a function of stellar host metallicity for known exoplanets in which we have distinguished those discovered by the transit method that

have measured masses (green circles) and those discovered by radial velocity only (black diamonds). For those planets with no detected transits, we plot the minimum mass ($M_p \sin i$) instead. In this plot we also show our four new discovered planets, highlighting the position of HATS-41 as the highest metallicity star hosting a planet with well characterised mass and radius. The clustering of planets below $4M_J$ masses in the above solar metallicity regime is clearly seen, despite the existence of a

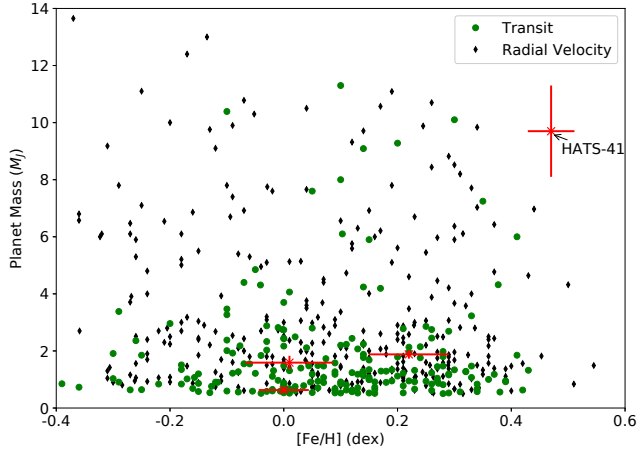


Figure 11. Planet Mass (or $M_p \sin i$) as a function of stellar metallicity for known exoplanets above $0.5M_J$ mass. We show two data sets; the first consists of planets originally discovered via the transit method (green circles) and which have reliable measured masses and radii. The second, corresponds to those discovered by Radial Velocity only (black diamonds) and, thus, the minimum mass value ($M_p \sin i$) is shown. We also show our new discovered planets, highlighting the case of HATS-41 as the highest metallicity host star with a known transiting planet to date.

significant number of low metallicity stars hosting low mass giant planets. However, for planets above this mass threshold, most transiting planets are still found to orbit stars with higher than solar metallicity, and the top-left region of the plot is dominated by planets found by radial velocity. Given the observational bias on the discovery of transiting planets favoring short period orbits, typically less than 20 days, these two samples are, in fact, somewhat different in nature as they represent planets with very different orbital periods. Therefore, while the statement is still true that planets above $4M_J$ masses have less of a dependence on metallicity, hot Jupiters are still found to follow the previous known relation. This suggests that the relation between giant planet mass and host star metallicity may also depend on the orbital period of the planet and that the inward migration process for giant planets that results in the known sample of hot Jupiters may be dependent on the host star properties. This is further evidence that the known sample of hot Jupiters is indeed distinct from the remaining planet population. A larger number of well characterised planets is required to further address this issue, and the advent of the next generation of instruments will improve our understanding of these processes.

Despite the fact that these new four exoplanets reside in relatively similar environments in terms of stellar host type and orbital separation (and thus similar equilib-

rium temperatures within a $\sim 500K$ range), they span effectively the entire mass range of known hot Jupiters, as show in Figure 10. We note that, given the large uncertainties in the radii of HATS-41b and HATS-42b (likely related to a combination of the limited precision on the stellar radius estimates and lack of extensive photometric follow-up), further observations are required to obtain improved estimates of this parameter for these targets. We therefore find them to be consistent with models of planetary radii under comparable equilibrium temperatures.

Development of the HATSouth project was funded by NSF MRI grant NSF/AST-0723074, operations have been supported by NASA grants NNX09AB29G, NNX12AH91H, and NNX17AB61G, and follow-up observations have received partial support from grant NSF/AST-1108686. J.H. acknowledges support from NASA grant NNX14AE87G. A.J. acknowledges support from FONDECYT project 1171208, BASAL CATA PFB-06, and project IC120009 “Millennium Institute of Astrophysics (MAS)” of the Millenium Science Initiative, Chilean Ministry of Economy. R.B. and N.E. acknowledge support from project IC120009 “Millennium Institute of Astrophysics (MAS)” of the Millennium Science Initiative, Chilean Ministry of Economy. V.S. acknowledges support form BASAL CATA PFB-06. This work also uses observations obtained with facilities of the Las Cumbres Observatory Global Telescope (LCOGT). This research has made use of the NASA Exoplanet Archive, which is operated by the California Institute of Technology, under contract with the National Aeronautics and Space Administration under the Exoplanet Exploration Program. This work is based on observations made with ESO Telescopes at the La Silla Observatory. Work at the Australian National University is supported by ARC Laureate Fellowship Grant FL0992131. We acknowledge the use of the AAVSO Photometric All-Sky Survey (APASS), funded by the Robert Martin Ayers Sciences Fund, and the SIMBAD database, operated at CDS, Strasbourg, France. Operations at the MPG 2.2m Telescope are jointly performed by the Max Planck Gesellschaft and the European Southern Observatory. We are grateful to P.Sackett for her help in the early phase of the HATSouth project. This research has made use of the NASA/ IPAC Infrared Science Archive, which is operated by the Jet Propulsion Laboratory, California Institute of Technology, under contract with the National Aeronautics and Space Administration. This work is based on observations collected with HARPS and FEROS at the European Organisation

for Astronomical Research in the Southern Hemisphere under ESO programmes 095.C-0367, CN2013A-171, CN2013B-55, CN2014A-104, CN2014B-57, CN2015A-51 and ESO 096.C-0544. This work has made use of data from the European Space Agency (ESA) mission

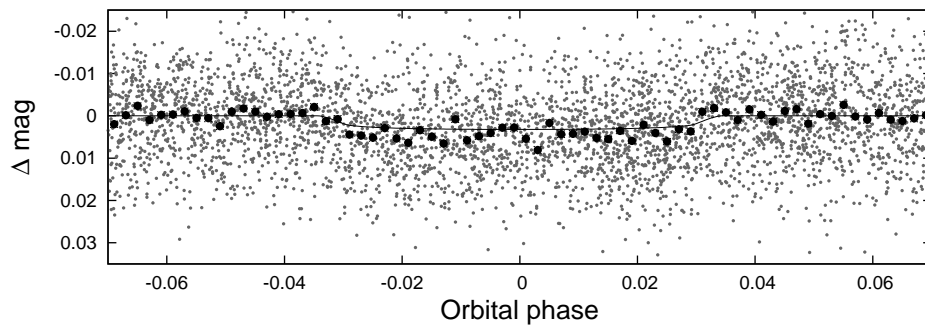
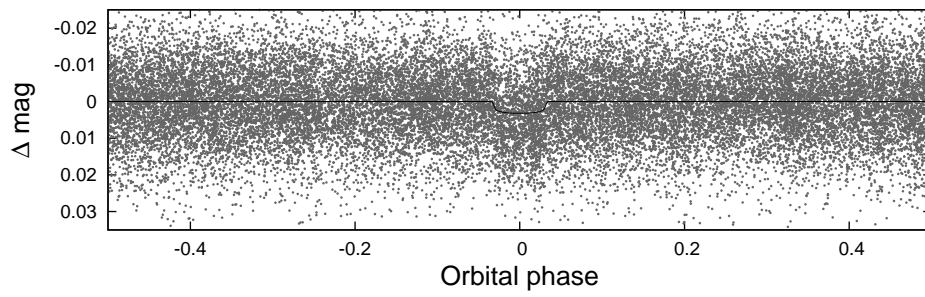
Gaia (<https://www.cosmos.esa.int/gaia>), processed by the *Gaia* Data Processing and Analysis Consortium (DPAC, <https://www.cosmos.esa.int/web/gaia/dpac/consortium>). Funding for the DPAC has been provided by national institutions, in particular the institutions participating in the *Gaia* Multilateral Agreement.

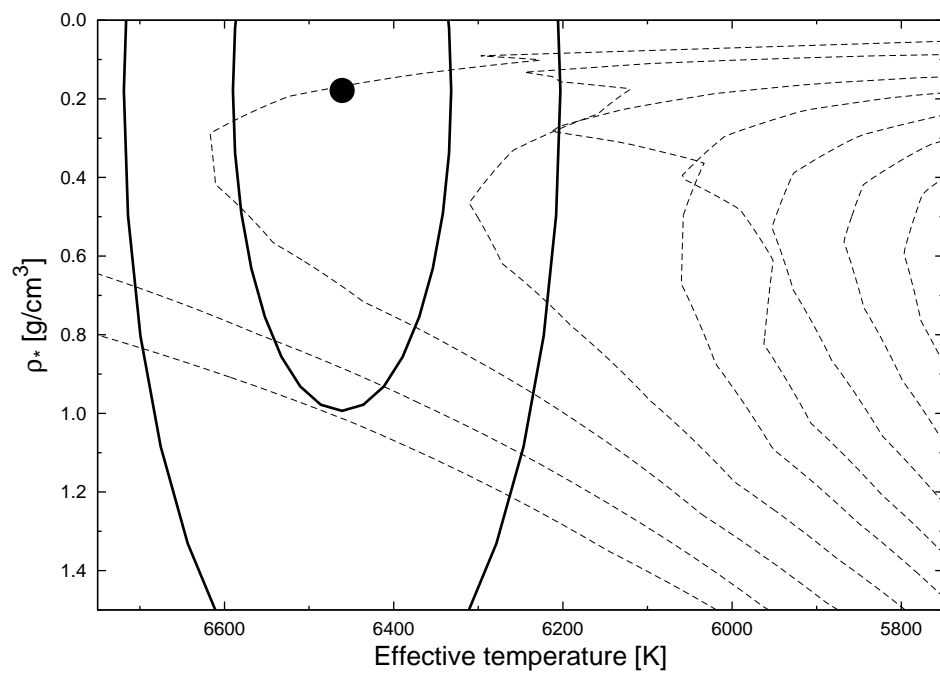
REFERENCES

- Addison, B. C., Tinney, C. G., Wright, D. J., et al. 2013, *ApJL*, 774, L9
- Akeson, R. L., Chen, X., Ciardi, D., et al. 2013, *PASP*, 125, 989
- Bakos, G., Noyes, R. W., Kovács, G., et al. 2004, *PASP*, 116, 266
- Bakos, G. Á., Torres, G., Pál, A., et al. 2010, *ApJ*, 710, 1724
- Bakos, G. Á., Csubry, Z., Penev, K., et al. 2013, *PASP*, 125, 154
- Bayliss, D., Zhou, G., Penev, K., et al. 2013, *AJ*, 146, 113
- Bayliss, D., Hartman, J. D., Bakos, G. Á., et al. 2015, *AJ*, 150, 49
- Bento, J., Wheatley, P. J., Copperwheat, C. M., et al. 2014, *MNRAS*, 437, 1511
- Borucki, W. J., Koch, D., Basri, G., et al. 2010, *Science*, 327, 977
- Boss, A. P. 1998, *ApJ*, 503, 923
- Brahm, R., Jordán, A., & Espinoza, N. 2017a, *PASP*, 129, 034002
- Brahm, R., Jordán, A., Hartman, J., & Bakos, G. 2017b, *MNRAS*, 467, 971
- Brahm, R., Jordán, A., Hartman, J. D., et al. 2015, *AJ*, 150, 33
- Brahm, R., Jordán, A., Bakos, G. Á., et al. 2016, *AJ*, 151, 89
- Brown, T. M., Baliber, N., Bianco, F. B., et al. 2013, *PASP*, 125, 1031
- Cameron, A. G. W. 1978, in *IAU Colloq. 52: Protostars and Planets*, ed. T. Gehrels, 453–487
- Cardelli, J. A., Clayton, G. C., & Mathis, J. S. 1989, *ApJ*, 345, 245
- Chambers, J. E. 2009, *ApJ*, 705, 1206
- Claret, A. 2004, *A&A*, 428, 1001
- Désert, J.-M., Charbonneau, D., Fortney, J. J., et al. 2011, *ApJS*, 197, 11
- Dopita, M., Hart, J., McGregor, P., et al. 2007, *Ap&SS*, 310, 255
- Espinoza, N., Bayliss, D., Hartman, J. D., et al. 2016, *AJ*, 152, 108
- Fischer, D. A., & Valenti, J. 2005, *ApJ*, 622, 1102
- Ford, E. B., & Rasio, F. A. 2008, *ApJ*, 686, 621
- Fortney, J. J., Marley, M. S., & Barnes, J. W. 2007, *ApJ*, 659, 1661
- Girardi, L., Bressan, A., Bertelli, G., & Chiosi, C. 2000, *A&AS*, 141, 371
- Gustafsson, B., Edvardsson, B., Eriksson, K., et al. 2008, *A&A*, 486, 951
- Hansen, B. M. S., & Barman, T. 2007, *ApJ*, 671, 861
- Hartman, J. D., Bakos, G. Á., Béky, B., et al. 2012, *AJ*, 144, 139
- Henden, A., & Munari, U. 2014, *Contributions of the Astronomical Observatory Skalnaté Pleso*, 43, 518
- Hippler, S., Bergfors, C., Brandner Wolfgang, et al. 2009, *The Messenger*, 137, 14
- Janson, M., Durkan, S., Hippler, S., et al. 2017, *A&A*, 599, A70
- Jordán, A., Espinoza, N., Rabus, M., et al. 2013, *ApJ*, 778, 184
- Jordán, A., Brahm, R., Bakos, G. Á., et al. 2014, *AJ*, 148, 29
- Kaufer, A., & Pasquini, L. 1998, in *Society of Photo-Optical Instrumentation Engineers (SPIE) Conference Series*, Vol. 3355, *Optical Astronomical Instrumentation*, ed. S. D’Odorico, 844–854
- Kennedy, G. M., & Kenyon, S. J. 2008, *ApJ*, 673, 502
- Kovács, G., Bakos, G., & Noyes, R. W. 2005, *MNRAS*, 356, 557
- Kovács, G., Zucker, S., & Mazeh, T. 2002, *A&A*, 391, 369
- Lindegren, L., Lammers, U., Bastian, U., et al. 2016, *A&A*, 595, A4
- Louden, T., & Wheatley, P. J. 2015, *ApJL*, 814, L24
- Mandel, K., & Agol, E. 2002, *ApJL*, 580, L171
- Mayor, M., Pepe, F., Queloz, D., et al. 2003, *The Messenger*, 114, 20
- Mazeh, T., Mayor, M., & Latham, D. W. 1997, *ApJ*, 478, 367
- Mizuno, H. 1980, *Progress of Theoretical Physics*, 64, 544
- Nayakshin, S. 2017, *MNRAS*, 470, 2387
- Pál, A., Bakos, G. Á., Torres, G., et al. 2008, *ApJ*, 680, 1450
- Penev, K., Bakos, G. Á., Bayliss, D., et al. 2013, *AJ*, 145, 5

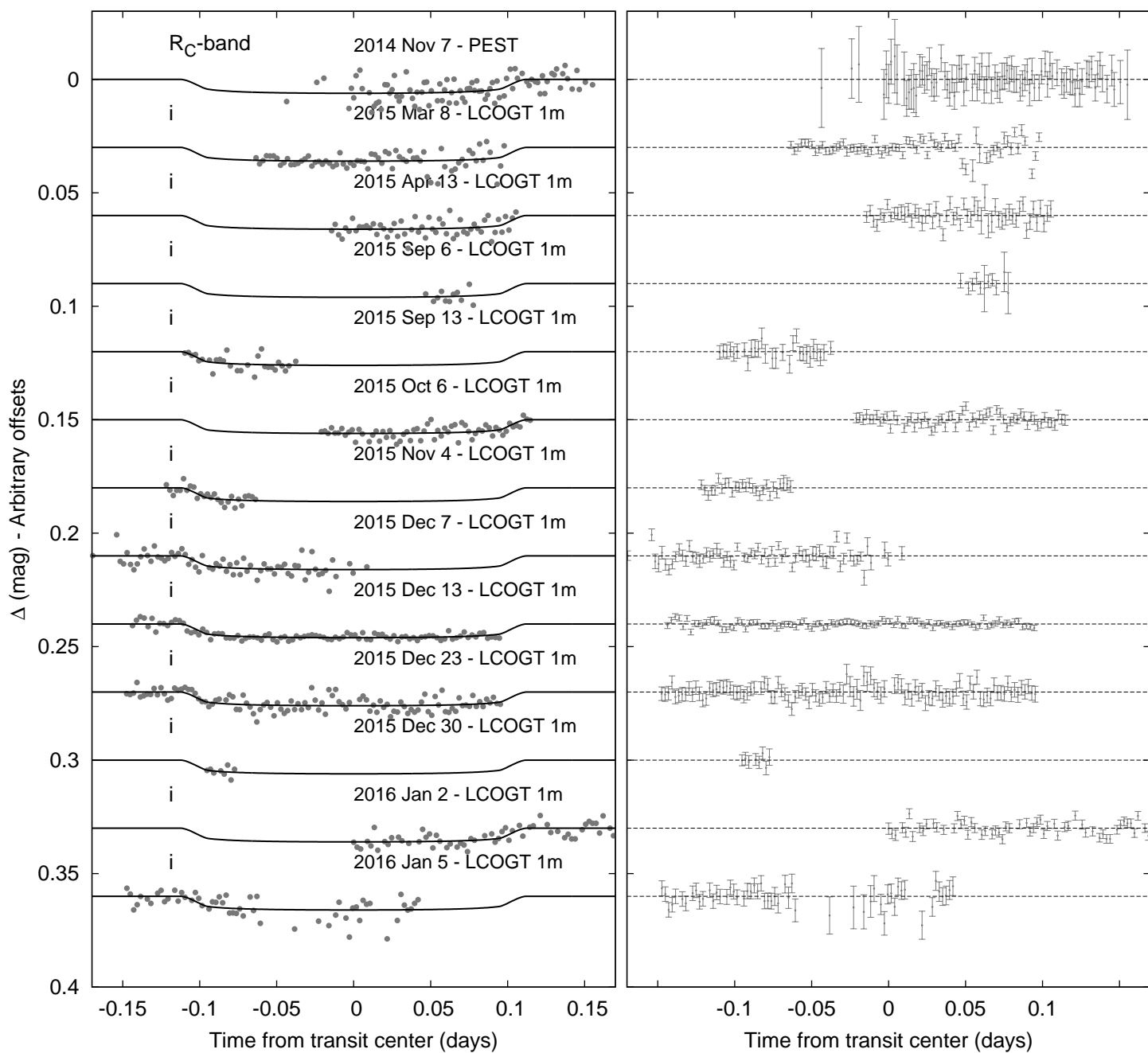
- Pepe, F., Ehrenreich, D., & Meyer, M. R. 2014, *Nature*, 513, 358
- Perri, F., & Cameron, A. G. W. 1974, *Icarus*, 22, 416
- Petrovich, C. 2015, *ApJ*, 805, 75
- Pollacco, D. L., Skillen, I., Collier Cameron, A., et al. 2006, *PASP*, 118, 1407
- Pont, F., Husnoo, N., Mazeh, T., & Fabrycky, D. 2011, *MNRAS*, 414, 1278
- Queloz, D., Mayor, M., Udry, S., et al. 2001, *The Messenger*, 105, 1
- Rabus, M., Jordán, A., Hartman, J. D., et al. 2016, *AJ*, 152, 88
- Rafikov, R. R. 2005, *ApJL*, 621, L69
- Santos, N. C., Israelian, G., & Mayor, M. 2004, *A&A*, 415, 1153
- Santos, N. C., Sousa, S. G., Mortier, A., et al. 2013, *A&A*, 556, A150
- Santos, N. C., Adibekyan, V., Figueira, P., et al. 2017, *A&A*, 603, A30
- Sing, D. K., Pont, F., Aigrain, S., et al. 2011, *MNRAS*, 416, 1443
- Southworth, J., Hinse, T. C., Dominik, M., et al. 2009, *ApJ*, 707, 167
- Sozzetti, A., Torres, G., Charbonneau, D., et al. 2007, *ApJ*, 664, 1190
- Weinberg, M. D., Yoon, I., & Katz, N. 2013, *ArXiv e-prints*, arXiv:1301.3156
- Wu, Y., & Murray, N. 2003, *ApJ*, 589, 605
- Yi, S., Demarque, P., Kim, Y.-C., et al. 2001, *ApJS*, 136, 417
- Zacharias, N., Finch, C. T., Girard, T. M., et al. 2012, *VizieR Online Data Catalog*, 1322, 0
- Zechmeister, M., & Kürster, M. 2009, *A&A*, 496, 577
- Zhou, G., Bayliss, D. D. R., Kedziora-Chudczer, L., et al. 2014, *MNRAS*, 445, 2746

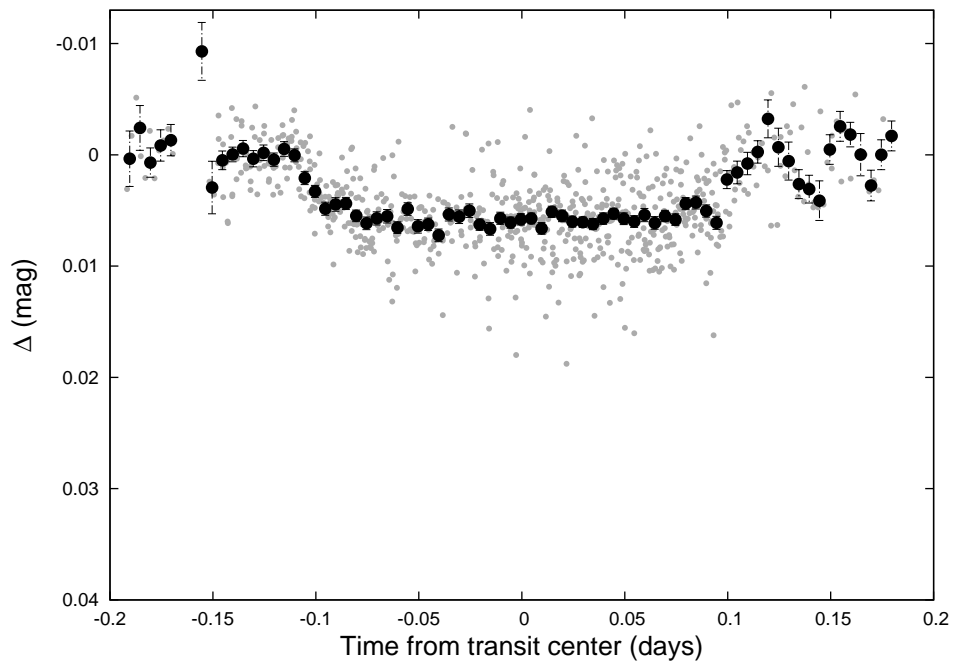
HATS-40





HATS-40





HATS-40

